CrossMark

JM PAPERS

Effect of plasma actuator-based control on flow-field and acoustics of supersonic rectangular jets

Anirudh Lakshmi Narasimha Prasad[1,†] **and S. Unnikrishnan**[1]

[1]Department of Mechanical Engineering, FAMU-FSU College of Engineering, Florida State University, Tallahassee, FL 32310, USA

We perform a computational study on the effects of localized arc filament plasma actuator based control on the flow field and acoustics of a supersonic 2:1 aspect ratio rectangular jet. Post validation of the baseline jet, effects of control in the context of noise reduction are studied at experimentally guided forcing parameters, including frequencies $St = 0.3$, 1.0 and $St = 2.0$ with duty cycles of 20 % and 50 %. In general, high-frequency forcing reduces noise in the downstream direction, with the actuator signature appearing mostly in the sideline direction. Here $St = 1$, $DC = 50\%$ yields an optimum balance between peak noise reduction (of $\sim$1.5 dB) and actuator tones, with control being most effective on the major axis plane that bisects the shorter edges of the nozzle. Shear layer response to the most effective forcing includes generation of successive arrays of mutually interacting staggered lambda vortices, which eventually energize streamwise vortical elements. Causal mechanisms of noise mitigation are further elucidated as follows. First, the control reduces the energy within the supersonic phase speed regime of peak radiating frequencies by redistributing a part of it into a high-frequency band. Second, it enhances azimuthal percolation of energy into the first and second helical modes at frequencies where noise reduction is seen, thus weakening the radiatively efficient axisymmetric mode. Finally, sound-producing intermittent events in the jet are significantly reduced, thereby minimizing the high-intensity acoustic emissions. This small-perturbation-based control strategy results in only minor variations in the mean flow properties. However, reduced production and enhanced convection attenuate turbulent kinetic energy within the spreading shear layer in the controlled jet.

Key words: jet noise, noise control, shear layer turbulence

† Email address for correspondence: al20di@fsu.edu

1. Introduction

Intense noise levels produced by high-speed military aircraft have an adverse impact on the personnel and surrounding structures. Noise levels are often above 120 dB (the human hearing pain threshold), which leads to physical and mental health problems, including hearing loss (Durch, Joellenbeck & Humes 2006; Helfer 2011; Yong & Wang 2015). These acoustic waves can also cause structural damage to surrounding buildings and aircraft control surfaces (Stephens & Mayes 1979). Thus, a study of jet noise and control strategies for noise reduction is vital.

There has been a renewed interest in the study of non-axisymmetric jets, in particular, those generated from rectangular nozzles, due to their superior air-frame integration properties and lower drag penalty (Wiegand 2018) in comparison to an axisymmetric nozzle. However, compared with axisymmetric designs, flow features of non-axisymmetric nozzles are more complex. For example, the influence of the aspect ratio (AR) of these nozzles results in a differential rate of core collapse between the two principal planes (major and minor axis), which can potentially affect far-field acoustic characteristics (Gutmark & Grinstein 1999). In addition, differential growth rates of shear layers in the two planes can produce a crossover point where axis switching can occur (Chen & Yu 2014; Valentich, Upadhyay & Kumar 2016). Axis switching can affect jet acoustics through enhanced large-scale mixing (Gutmark & Grinstein 1999). Sharp corners inherent to these nozzle geometries cause the formation of corner vortices, which can aid mixing, and influence growth of coherent structures in the flow (Zaman 1996). Additional features such as warping of azimuthal vortices (Grinstein 1995) and preferential flapping about the minor axis plane (Gutmark, Schadow & Bicker 1990; Shih, Krothapalli & Gogineni 1992) can also induce additional noise production mechanisms, rendering the flow field and acoustics of these jets significantly different from the widely studied circular jets.

In spite of the above differences, far-field acoustics of rectangular jets share some similarities with those of axisymmetric jets at low AR (typically below 4 : 1) (Bridges 2012; Heeb *et al.* 2013; Chakrabarti, Gaitonde & Unnikrishnan 2021). Specifically, the downstream shallow angle acoustic radiation exhibits axisymmetric behaviour, due to the dominance and radiative efficiency of lower azimuthal modes (Michalke & Fuchs 1975). Although the plume largely maintains the nozzle shape near the exit, corner instabilities amplify downstream, making the plume increasingly axisymmetric. It has to be noted that the above trends are primarily associated with perfectly expanded jets. Imperfect expansion and the presence of shocks (Veltin & McLaughlin 2009) or the dominance of a flapping mode (Gojon, Gutmark & Mihaescu 2019) can induce significant flow and acoustic asymmetry even in low-AR jets.

To mitigate the acoustic impact of these jets, both passive and active control strategies have been pursued. Commonly studied passive control devices include chevrons and tabs/vortex generators. Chevrons are effective in reducing low frequency noise in mid- to high-subsonic conditions (Martens 2002) and have been implemented in commercial turbofan engines. Vortex generators have shown promise with peak noise reduction in the far field for supersonic jets exiting a circular nozzle (Liu *et al.* 2021, 2022). Versatility of active control techniques makes them an attractive choice for military aircraft that operate in a wide range of temperature and expansion ratios. Micro-jets (Alvi *et al.* 2008) or fluidic inserts (Coderoni, Lyrintzis & Blaisdell 2019; Prasad & Morris 2020) have been extensively studied in this regard, due to their ability to enhance mixing in the shear layer through the introduction of streamwise vortices. These techniques have been effective in reducing noise levels along certain planes

of a nozzle and in suppressing tonal noise components. Plasma actuators (Samimy *et al.* 2007*a*) are another category of active control techniques that leverage instabilities in the jet shear layer to amplify perturbations imposed near the nozzle lip, thus altering the evolution of coherent structures in the flow, and eventually reducing noise levels.

The current study pertains to the application of localized arc filament plasma actuator (LAFPA) based control of supersonic rectangular jets. Due to their capability to operate at high frequencies (in the range of 100 kHz) (González, Gaitonde & Lewis 2015) they have been extensively utilized for noise control of high-speed jets (Samimy *et al.* 2007*a*,*b*). When applied close to the nozzle exit where the jet shear layer is highly susceptible to small perturbations, LAFPAs influence Kelvin–Helmholtz instabilities to amplify perturbations into large scale coherent structures. Based on actuator parameters including frequency, duty cycle and azimuthal mode, the resulting flow structures display varying growth/decay rates and spatiotemporal evolution, ultimately influencing the acoustic characteristics of the flow.

Experiments (Samimy *et al.* 2007*a*,*b*; Samimy, Kim & Kearney-Fischer 2009; Samimy *et al.* 2010) and computations (Gaitonde & Samimy 2010, 2011) on circular jets highlight the importance of the spectral signature and intermittent nature of the actuators in influencing the jet flow field. Acoustic measurements by Samimy *et al.* (2009, 2010) showed that LAFPA actuation at the column mode of the jet (Crow & Champagne 1971; Kibens 1980) amplifies the super-directive acoustic radiation leading to increased peak noise levels in both the near field and far field. Corresponding simulations (Gaitonde 2012) identify the formation of large-scale coherent toroidal vortical structures in the flow. Speth & Gaitonde (2013) observed that duty cycle variations spanning 20 % to 90 % had minimal effects on the flow-field response of circular jets. However, with increased azimuthal modes ($m = 1$ and 2) of forcing, the plumes generated single and double helical vortex streams. Samimy *et al.* (2009, 2010) demonstrated on circular jets that LAFPA-based control is an effective noise reduction mechanism. They identified an optimum forcing frequency range between $St \sim 0.8$ to $St \sim 1.5$, where a broadband reduction in peak noise levels was achieved at downstream radiating angles. These experiments highlight the necessity to control the size of structures produced, limit their spatial extent of growth and reduce interactions between structures to obtain effective noise reduction using plasma actuators.

While there is a substantial amount of work on LAFPA-based control of circular jets, its effects on rectangular jets are relatively less explored. Some published works include that of Snyder (2007) who assessed the mixing characteristics of rectangular jets forced by LAFPA actuators. Recently, Ghassemi Isfahani, Webb & Samimy (2022) and Leahy *et al.* (2022) conducted experiments to study screech and coupling modes of twin rectangular jets at various Mach numbers. Furthermore, the existing computational studies on LAFPA-based control primarily focus on the near-field characteristics in these controlled jets.

To address the above aspects, we present a computational analysis of a perfectly expanded rectangular supersonic jet, controlled by a LAFPA-based actuator. Major objectives of this study are as follows.

(i) Evaluate the impact of LAFPA-based actuators on rectangular supersonic jets for noise control, utilizing a high-fidelity simulation framework.
(ii) Identify causal mechanisms that determine the controlled response of the jet, including fundamental shear layer dynamics and variations in the acoustic gain.

We expect this analysis to provide insights into small-perturbation-based scalable noise control strategies for non-axisymmetric jets by targeting the most significant events that generate acoustic emissions.

The following outlines our presentation. The geometric details, Navier–Stokes solver, grid and actuator parameters are explained in § 2. We choose a benchmark rectangular jet flow field with AR = 2 : 1, which is validated using published data in § 3. Characteristics of the baseline (no-control) case are also provided here. Effects of forcing parameters including frequency and duty cycle on the near-field flow features and far-field acoustics are reported in §§ 4.1 and 4.2, respectively. The observed acoustic trends are connected to fundamental shear layer dynamics and acoustic gain of the jets in §§ 5 and 6, respectively. Finally, § 7 details the effects of control on the mean flow and turbulent statistics.

2. Solver set-up and simulation parameters

Computations solve the three-dimensional compressible Navier–Stokes equations in generalized curvilinear coordinates using an implicit large-eddy simulation (LES) framework, using the formulation

$$\frac{\partial}{\partial \tau}\left(\frac{\boldsymbol{Q}}{J}\right) = -\left[\left(\frac{\partial \boldsymbol{F_i}}{\partial \xi} + \frac{\partial \boldsymbol{G_i}}{\partial \eta} + \frac{\partial \boldsymbol{H_i}}{\partial \zeta}\right) + \frac{1}{Re}\left(\frac{\partial \boldsymbol{F_v}}{\partial \xi} + \frac{\partial \boldsymbol{G_v}}{\partial \eta} + \frac{\partial \boldsymbol{H_v}}{\partial \zeta}\right)\right], \qquad (2.1)$$

where $\boldsymbol{Q} = [\rho, \rho u, \rho v, \rho w, \rho E]^{\mathrm{T}}$ is the vector of conserved variables, where ρ is the density, and (u, v, w) are velocity components in Cartesian coordinates. The total specific internal energy is given by $E = T/[\gamma(\gamma - 1)M_j^2] + (u^2 + v^2 + w^2)/2$, where T is temperature, γ is the ratio of the specific heats and $M_j = 1.5$ is the reference jet Mach number at the nozzle exit. Here $J = \partial(\xi, \eta, \zeta, \tau)/\partial(x, y, z, t)$ is the Jacobian, $(\boldsymbol{F_i}, \boldsymbol{G_i}, \boldsymbol{H_i})$ denote the inviscid fluxes while $(\boldsymbol{F_v}, \boldsymbol{G_v}, \boldsymbol{H_v})$ denote the viscous fluxes, along the computational coordinates, (ξ, η, ζ), respectively. The system of equations is closed using the ideal gas law, $p = \rho T/\gamma M_j^2$, while assuming a constant Prandtl number of $Pr = 0.72$. Effects of temperature on viscosity are modelled using Sutherland's law. Further details of the formulation are available in Garmann (2013).

In the following description starred quantities ($\{\cdot\}^*$) denote dimensional variables. All primitive variables except pressure are non-dimensionalized by their corresponding values at the jet exit. Here $p = p^*/\rho_j^* U_j^{*2}$ is defined as the non-dimensional pressure. Based on the equivalent diameter of the rectangular nozzle, D_{eq}^*, (further explained in the subsequent section), the Reynolds number is defined as $Re = \rho_j^* U_j^* D_{eq}^*/\mu_j^*$. Non-dimensional time is defined as $t = t^*/T_C^*$, where $T_C^* = D_{eq}^*/U_j^*$ is the characteristic time scale. Non-dimensional frequency, commonly referred to as Strouhal number, is defined as $St = f^* D_{eq}^*/U_j^*$, where f^* is the dimensional frequency in Hz.

Convective fluxes are reconstructed using a seventh-order weighted essentially non-oscillatory scheme (Liu, Osher & Chan 1994) in the smooth regions of the flow. The Roe scheme (Roe 1981) is then used to evaluate interface fluxes. Viscous fluxes are discretized using second-order central difference. Time integration is performed using a nonlinearly stable third-order Runge–Kutta scheme (Shu & Osher 1988).

The orthogonal grid (shown in figure 1a) consists of $\sim 47.53 \times 10^6$ nodes, and is discretized using 511 nodes along the streamwise direction, and 309 and 301 nodes along the directions corresponding to the shorter and longer edges of the nozzle, respectively. Grid refinement is provided near the nozzle walls and exit, with a minimum wall-normal spacing, $\Delta n \sim 0.001$. Typical grid spacing in the plume is $\Delta x \sim 0.025$, while the
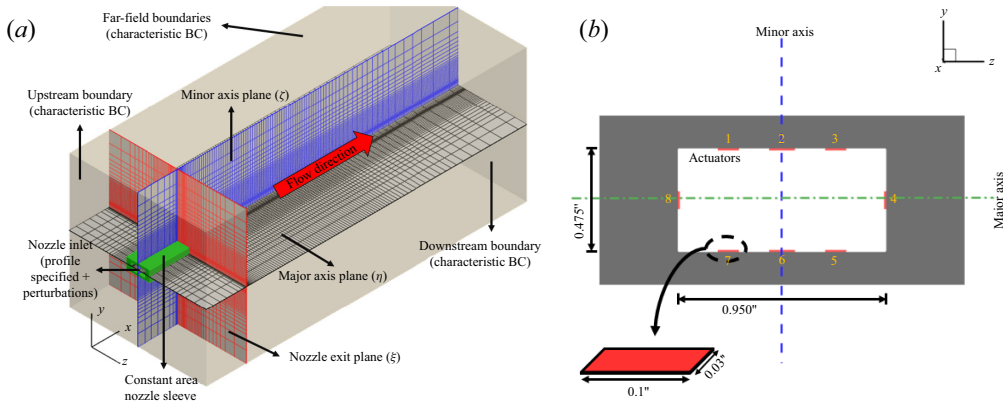
Figure 1. (*a*) Principal planes of the computational domain and the boundary conditions utilized in the simulations. Every fourth node is shown. (*b*) Schematic of the nozzle and actuators. Nozzle and actuator dimensions, and principal planes are also shown.

transverse grid spacing near the shear layer is $\Delta y, \Delta z \sim 0.001$. Stretched grids near outflow boundaries minimize numerical reflections into the domain. The computational domain extends to $\sim 30 D_{eq}$ in the streamwise direction and $\sim 12 D_{eq}$ along the other two orthogonal directions. These parameters are informed by prior studies (Chakrabarti *et al.* 2021) on supersonic rectangular jets at comparable *Re*. A grid convergence study is also performed to assess the effects of mesh resolution on the plume of the baseline jet by comparing results from a coarse and fine grid. Details of this study are summarized in the Appendix. Based on this, the following results are computed on the finer grid.

The simulated flow fields correspond to a Mach 1.5 (design Mach number) jet, exiting from a rectangular nozzle. The nozzle has an AR of 2 : 1, with dimensions of 0.950 inches (24.13 mm) along the longer edge and 0.475 inches (12.06 mm) along the shorter edge (see figure 1*b*). These dimensions correspond to that reported in Isfahani, Webb & Samimy (2021). The nozzle is modelled as a constant-area sleeve with a streamwise length, 3.67 equivalent diameters. The nozzle sleeve is visualized in figure 1(*a*). In this study the major axis plane is defined as the plane perpendicular to the shorter edges, and the minor axis plane as that perpendicular to the longer edges. The equivalent diameter of the rectangular jet is defined as $D_{eq}^* = \sqrt{(4/\pi) \times A_{exit}^*} = 0.758$ inches (19.25 mm). This is the equivalent diameter of a circular nozzle with an exit area the same as that of the rectangular nozzle. Based on the above reference quantities, $Re = \rho_j^* U_j^* D_{eq}^* / \mu_j^* \sim 1.09 \times 10^6$.

In the current study the Mach 1.5 jet is perfectly expanded and operates at a nozzle pressure ratio (ratio of stagnation pressure, p_o^*, to ambient pressure) of 3.67. The exiting jet is unheated at a velocity $u_{jet}^* = 424.74 \text{ m s}^{-1}$ and static temperature $T_{jet}^* = 224 \text{ K}$. The ambient pressure is $p_\infty^* = 101.325 \text{ kPa}$ and the temperature is $T_\infty^* = 300 \text{ K}$. The free-stream flow outside the nozzle imposes a small streamwise velocity of $u_\infty^* = 0.01 \times u_{jet}^*$ in order to effectively implement characteristic boundary conditions. The boundary conditions are also detailed in figure 1(*a*). Characteristic boundary conditions (Poinsot & Lele 1992; Blazek 2001) are imposed on all outer boundaries outside the nozzle. To minimize reflections, along with grid stretching, the order of reconstruction is also reduced locally near the outer boundaries. The nozzle surfaces are treated as no-slip adiabatic walls. On the inlet boundary within the nozzle block, the computations impose Dirichlet inflow conditions, similar to Bogey & Bailly (2010). Based on experimental estimates (Samimy
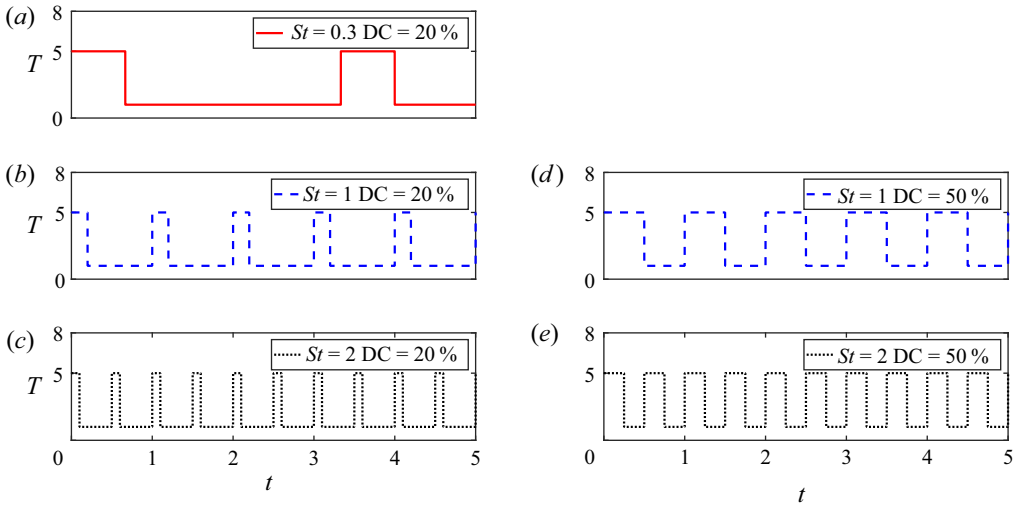
964 A11-5

Figure 2. Temporal variation of imposed excitation for cases shown in table 1; (*a–c*) 20 % duty cycle and (*d,e*) 50 % duty cycle.

et al. 2007*a*), the exiting boundary layers in these high-speed jets are around 1 mm in thickness. Therefore, velocity and density profiles corresponding to a boundary layer thickness $\delta_{99} \sim 0.85$ mm are utilized. To aid development of stochastic perturbations in the shear layer, spatiotemporally correlated 'coloured' pressure perturbations are imposed on the boundary layer (Adler *et al.* 2018), and is allowed to develop over the length of the nozzle sleeve before exiting into the ambient. This leads to a broadband spectra within the boundary layer and subsequently in the shear layer. A non-dimensional time step of $\Delta t^*/T_C^* = 5 \times 10^{-4}$ is used for time integration. In all the simulations time-accurate data are obtained for 200 characteristic time intervals (T_C^*) at a sampling rate of $St = 20$. This was found sufficient for convergence of first- and second-order statistics in the turbulent plume, and far-field acoustic predictions, which was verified using multiple sampling lengths of the data. The reported overall sound pressure level (OASPL) is calculated by integrating the power spectral density between $0.05 \leq St \leq 1.5$.

The LAFPA actuator is modelled as a surface heating condition, based on prior computational studies (Gaitonde & Samimy 2011). Eight actuators are considered in this study, arranged around the nozzle inner wall close to the exit. Three actuators each are present along the longer edges of the nozzle, placed equidistant from the walls as well as each other (see figure 1*b*). One actuator each is present at the centre along the two shorter edges of the rectangle. Each actuator surface has dimensions of $0.1''(2.5\text{ mm}) \times 0.03''(0.75\text{ mm})$ ($l \times b$). The centre of each actuator is located $0.0569''(1.44\text{ mm})$ from the nozzle exit. These are based on corresponding LAFPA model dimensions tested on circular jets (Gaitonde 2012). When the actuator is on, the local surface temperature increases to $T = 5T_\infty$, which is informed by spectroscopic temperature measurements from experiments (Samimy *et al.* 2009; Gaitonde & Samimy 2010).

In the present study, in addition to the baseline case, we evaluate five types of actuation involving various spectral and duty cycle combinations, which are some of the most significant parameters affecting the response of the jet. These are tabulated in table 1. The choice of these parameters are influenced by their significance identified in the previously mentioned LAFPA-based experiments. While $St = 0.3$ allows us to study the

964 A11-6

Frequency (St)	0.3	1.0	2.0
Frequency (kHz)	6.62	22.06	44.13
Duty cycle (%)	20	20/50	20/50

Table 1. Forcing frequencies and duty cycles.

forced response to the most sensitive input near the column mode of the jet, $St = 1$ is representative of an effective frequency range for LAFPA control. Here $St = 2$ will provide insights on the shear layer response to relatively higher frequencies outside the dominant shear layer spectrum. Figure 2 plots the temperature signature of the actuators in the above cases. The abscissa is non-dimensional time, t, and the ordinate is normalized temperature (T/T_∞). Forcing frequency specifies the number of actuation cycles per unit non-dimensional time, while the duty cycle determines the duration within an actuation cycle over which the actuator is on. For example, a frequency of $St = 2$ has the actuator switching on and off twice per unit non-dimensional time, and a duty cycle of 50 % indicates that the actuator is switched on for 50 % of each cycle. To simplify the parameter space, we limit the evaluation to 'axisymmetric' excitation, where all eight actuators operate in identical phase. For notational convenience, in the following the duty cycle will be referred to as 'DCX', where 'X' refers to the duty cycle percentage. It has to be noted that for $St = 0.3$ forcing, only a single duty cycle is tested, since it results in significant increases in far-field noise levels due to the amplification of the column mode in the jet plume.

3. Baseline characteristics and validation

The flow field of the baseline jet is visualized in figure 3. It highlights vortical structures in the turbulent plume using an isolevel of Q criterion, coloured by streamwise velocity (u). Close to the nozzle exit, thin spanwise roller vortices are evident that experience a higher convective velocity along the inner shear layer region, as depicted by the colouring. As the shear layer spreads, these spanwise vortices transform into horse-shoe vortices that dominate the plume, until about the core collapse location. Further downstream, streamwise elongated vortex tubes are predominant. Turbulent mixing eventually leads to disintegration of coherent vortices into smaller scale structures.

We now validate the baseline simulation using published data on mean flow-field parameters and acoustic signature of the jet. The centreline mean velocity is plotted in figure 4(*a*) for jets operating under comparable conditions. The current result is denoted 'current study' and is compared with computational data of a Mach 1.5, AR $= 2 : 1$ rectangular jet, available in Viswanath *et al.* (2016), and that from simulations of an AR $= 3 : 1$ rectangular jet, reported in Seror *et al.* (2000). In addition, experimental data of an AR $= 3 : 1$ rectangular jet compiled by Kinzie (1995) are also included. While the AR $= 2 : 1$ is a non-method-of-characteristics (MOC) convergent-divergent (CD) nozzle, the latter CD nozzles (with AR $= 3 : 1$) have diverging sections designed using MOC, and are hence chosen for comparison. The current computations show a relatively closer match with the experimental data and computations by Seror *et al.* (2000) for the AR $= 3 : 1$ rectangular nozzle. The core collapse location ($x \sim 5.8$) and rate of velocity decay due to entrainment also compare well with the above data. Weak oscillations of the centreline velocity in the current study is due to a slight pressure
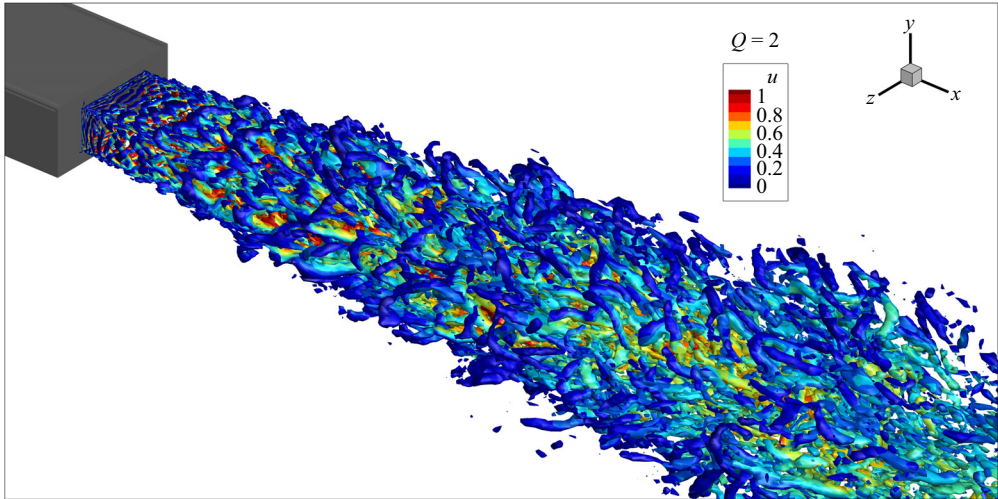
Figure 3. Instantaneous snapshot of the baseline jet. Vortical features are highlighted using isolevels of the Q criterion, coloured by streamwise velocity.
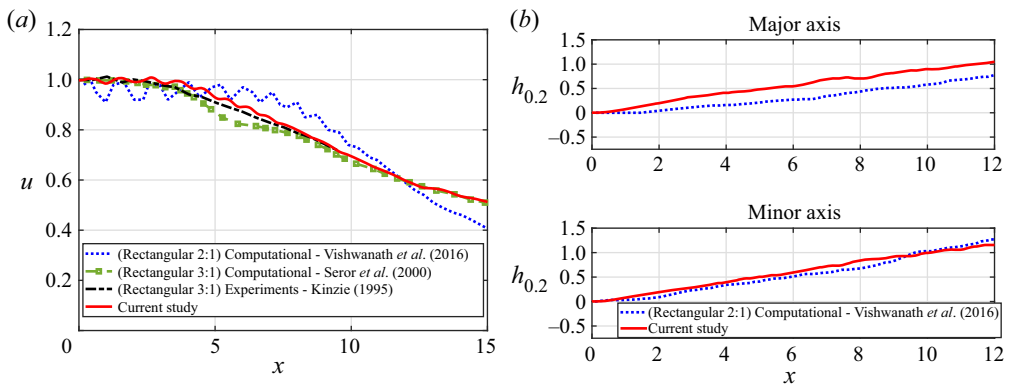

Figure 4. (*a*) Centreline velocity comparison. (*b*) Spreading-rate comparison on minor axis plane.

mismatch between the ambient and nozzle flow, resulting from the flow development within the nozzle block. The difference in current computations and that of Viswanath *et al.* (2016) is due to the presence of shock-expansion cells induced by the non-MOC design of the nozzle diverging section in the latter. Comparisons with circular jets at similar operating conditions (not included in the figure) also indicated that the rate of collapse of the potential core is higher in the rectangular jet when compared with a circular jet operating at similar conditions, consistent with prior studies (Chakrabarti *et al.* 2021). This is due to the relative proximity of shear layers developing along the longer edges of the nozzle (i.e. shear layers visible on the minor axis plane in the current convention).

To quantify the spreading rate of the jet, we utilize the transverse location where the mean streamwise Mach number ($\overline{M_x}$) attains a value, $\overline{M_x} = 0.2$, following the convention in Viswanath *et al.* (2016). This is plotted as $h_{0.2}$ in figure 4(*b*), on the two principal planes, for the current study and computations by Viswanath *et al.* (2016). A reasonable match is observed on the minor axis plane between the two. The variation on the
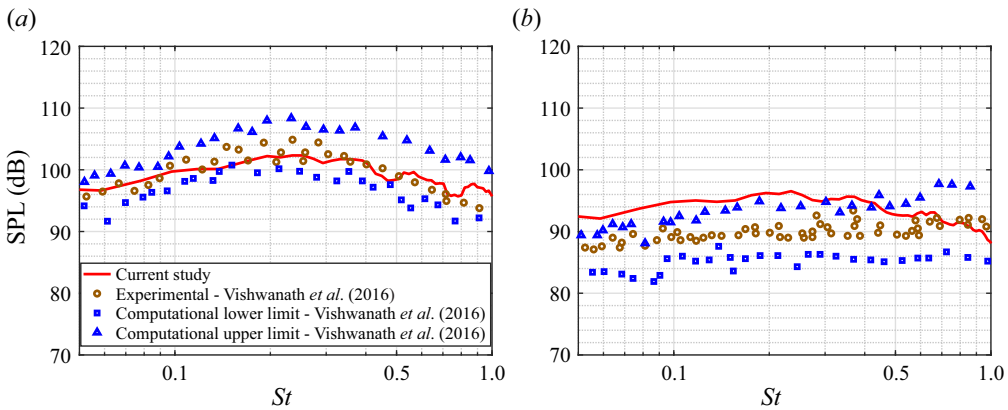
964 A11-8

Figure 5. Far-field SPL comparison at polar angles of (*a*) 36° and (*b*) 80° on the minor axis plane.

major axis plane is primarily due to the delayed initiation of spreading of the shear layer in the reference calculation, which can be attributed to the shock train at the nozzle exit. However, downstream of $x \sim 2$, the spreading rate is comparable between the two computations, as suggested by the two curves being almost parallel to each other.

The far-field signature of the baseline jet obtained from the acoustic field is shown at a location of $r = 40$ on the minor axis plane in figure 5. The far-field acoustic signature is obtained by first performing an acoustic filtering (Unnikrishnan & Gaitonde 2016), as detailed in § 5.2. The filtered acoustic fluctuations from a cylindrical surface at $r = 2.5$ are then propagated into the far field using a time-domain linear wave propagator. Details about the associated theory, implementation and validation have been published by Unnikrishnan, Cavalieri & Gaitonde (2019). For spectral calculations, the minimum bin is $St = 0.01$, and the Welch method (Welch 1967) is utilized with the signal segmented into five windows with 75 % overlap, consisting of 2048 points. This is compared with microphone data from experiments at the University of Cincinnati, and the corresponding computations, reported in Viswanath *et al.* (2016). Figure 5(*a*) shows the sound pressure level (SPL) comparison at a polar angle of $\theta = 36°$, measured from the jet downstream direction, and roughly corresponds to the direction of peak radiation of the jet. The acoustic spectra of the current study matches very well with experimental data and lies in between the upper and lower envelopes of the spectral predictions from the reference computations. As expected from a perfectly expanded jet, the noise spectra is mostly broadband, with relatively lower energy at higher frequencies. There exists a broadband energy peak at low-to-mid band frequencies between $0.2 \le St \le 0.4$ (4.4 kHz $\le f \le$ 8.8 kHz), corresponding to the column mode of the jet. This trend is consistent with the universal F-spectrum mixing noise curve identified by Tam, Golebiowski & Seiner (1996). Figure 5(*b*) shows the SPL comparison at a polar angle of $\theta = 80°$, which is along the jet sideline. There is a good match at higher frequencies, and some over-prediction at lower frequencies. This may be attributed to the differences in characteristics of fine-scale turbulence (Tam, Pastouchenko & Viswanathan 2005; Tam 2019) of the jet shear layers between the current study and reference studies, which is caused by the dissimilarities in the boundary layer characteristics exiting the nozzle (Brès *et al.* 2018). The flat broadband spectral shape is also consistent with the G-spectrum mixing noise curve proposed by Tam *et al.* (1996).

4. Acoustic impact of control

Since noise mitigation is a major consideration in LAFPA-based control of jets, we first detail the near-field and far-field acoustic impact of control. As discussed in § 2, the parameters considered here are the frequency and duty cycle of excitation.

4.1. *Effect of forcing frequency*

Depending on the forcing frequency, the jet may respond by energizing the large-scale coherent structures resulting in noise amplification, or reducing peak noise levels by redistribution of acoustic energy to off-peak frequencies or non-radiating wave speeds. To isolate the effect of forcing frequency, the duty cycle is fixed at 20 % (DC20) in this section, where we first describe the near-field trends in the LES domain, followed by the far-field acoustic signature.

4.1.1. *Near-field impact*

The phase-averaged acoustic near-field is presented in figure 6 using contours of dilatation ($\nabla \cdot \boldsymbol{u}$) for the baseline and controlled cases. Phase averaging on the controlled cases is performed by considering one cycle of the respective forcing frequency to be the reference signal. Since the baseline jet has no associated unique forcing signal, phase averaging is performed at all three frequencies ($St = 0.3$, 1 and $St = 2$) in order to compare with the controlled cases. The first snapshot obtained after attaining statistical stationarity of the simulation is considered as the beginning of the phase cycle in the baseline case.

The results presented correspond to a phase of π within each phase-averaged cycle. Bottom panels in figure 6(*a,c,e*) show phase-averaged dilatation contours on the major axis plane of the jet, corresponding to forcing at $St = 0.3$, 1 and $St = 2$, respectively. The same is shown for the minor axis plane in figure 6(*b,d,f*). The upper panel in each subfigure is the baseline jet phase averaged at the corresponding frequency.

Dilatation contours of the baseline jet phase averaged at $St = 0.3$ (figure 6*a,b*) show strong directive acoustic radiation at an angle of $\theta \sim 30°$, which roughly corresponds to the angle at which peak OASPL ($\sim$129 dB) is observed on both principal planes, consistent with experiments of Heeb *et al.* (2013). The directivity of this radiating stream is highlighted by a red line segment. Since the column mode of the jet exists in the spectral vicinity of $St = 0.3$ (Crow & Champagne 1971; Kibens 1980; Petersen & Samet 1988), this forcing produces the strongest response from the jet, as also seen in experiments by Samimy *et al.* (2007*a*). Here $St = 0.3$ forcing causes the naturally occurring directional radiation to intensify, leading to a significant increase in peak OASPL at $\theta \sim 34°$, and also elevated noise levels across polar angles. The acoustic waves have a periodic fish bone pattern similar to that observed by Gaitonde (2012) in their simulations of axisymmetric jets. The intensity of acoustic waves generated by forcing at $St = 0.3$ is higher on the minor axis plane than on the major axis plane. Comparison of the root-mean-square (RMS) pressure fluctuations at a distance of $y/z = 2.5$ from the nozzle lip line on the two principal planes showed that, along shallow angles measured with respect to the jet lip line ($\theta \sim 25°$), the pressure fluctuations on the minor axis plane were up to 22 % higher than that on the major axis plane.

The phase-averaged dilatation field of the baseline jet with $St = 1$ as the reference signal (figure 6*c,d*) shows very weak acoustic radiation, consistent with the roll-off in acoustic energy at higher frequencies. The controlled jet responds to forcing at this frequency by producing two dominant streams of acoustic radiation on the minor axis plane. The first stream is predominantly downstream, eventually spreading across the plane of propagation
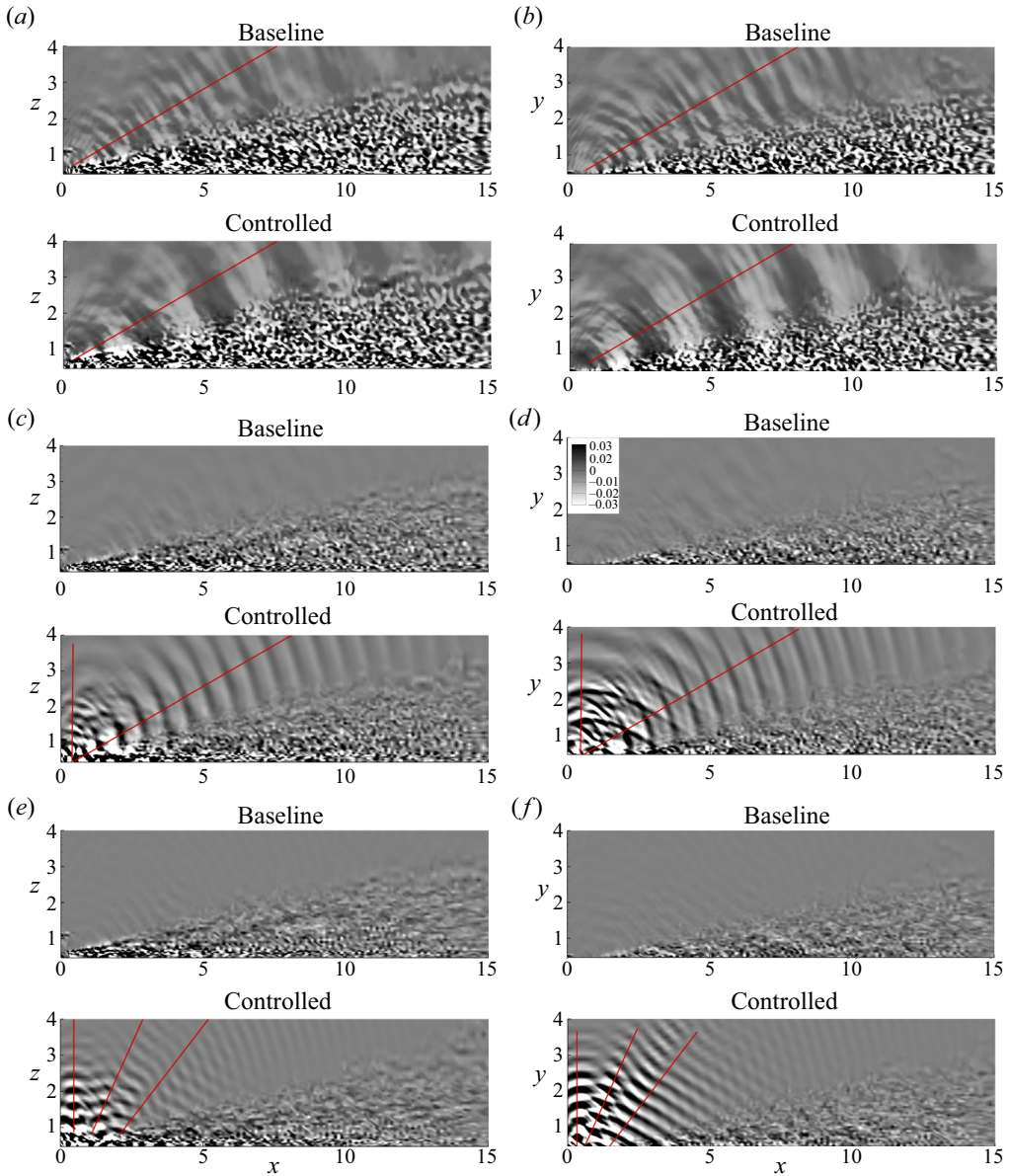
Figure 6. Phase-averaged dilatation contours of baseline (upper) and controlled (lower) cases corresponding to $St = 0.3$ on the (*a*) major axis plane and (*b*) minor axis plane. Corresponding results for (*c*,*d*) $St = 1$ forcing and (*e*,*f*) $St = 2$ forcing.

within $20° \leq \theta \leq 60°$. As a consequence, the downstream direction experiences additional radiation that was not present in the baseline case. This is induced by intrusion of vortical structures into the potential core, as shown in the phase-averaged flow field in figure 7(*a*).

Energy dynamics of such intrusion events and associated acoustic radiation have been detailed in Unnikrishnan & Gaitonde (2016). This is further analysed using the cross-correlation of acoustic fluctuations ($-\partial \psi'_a/\partial x$) (Unnikrishnan & Gaitonde 2016) and vorticity fluctuations (ω'_z). Acoustic fluctuations are obtained at $x = 3.7$ from the nozzle
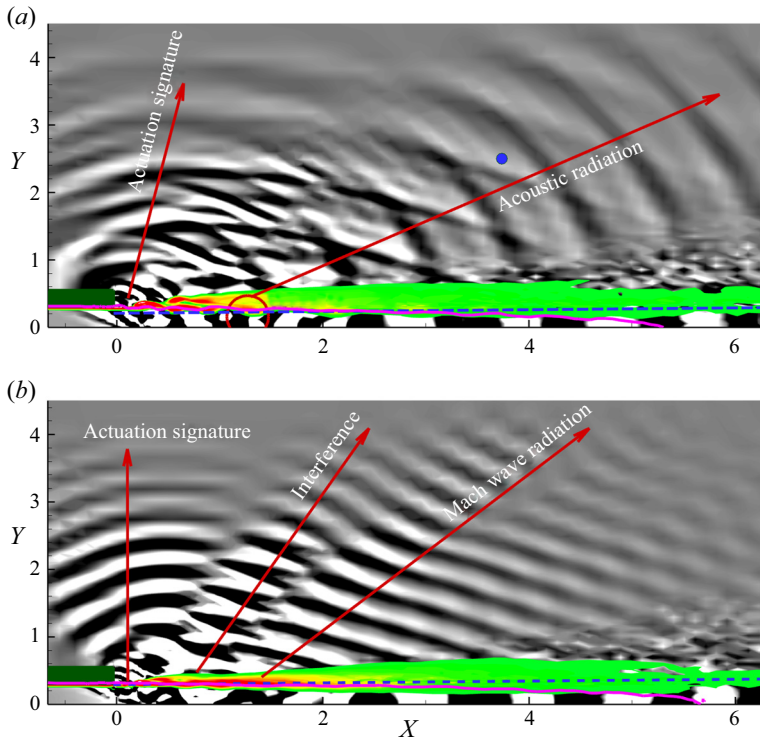
Figure 7. Phase-averaged vorticity and corresponding dilatation contours at a phase of π in the near nozzle regions for (*a*) $St = 1$ and (*b*) $St = 2$ actuation on the minor axis plane. The blue dot in (*a*) represents the point where the time trace of acoustic fluctuations $(-\partial \psi'_a/\partial x)$ are extracted, while the dashed blue line represents the series of spatial locations over which the time trace of vorticity fluctuations (ω'_z) are extracted. The dashed blue line in (*b*) represents the location where *x-t* variation of vorticity fluctuations (ω'_z) are studied. Potential core outlines using the $u = 0.9$ contour, represented by the pink solid line.

exit, and $y = 2.5$ from the centreline, corresponding to a polar angle of $\theta \sim 34°$, and is denoted by a blue dot in figure 7(*a*). Vorticity fluctuations are obtained along a horizontal line, $y = 0.2$, from the centreline. Figure 8(*a*) shows the cross-correlation contours where the abscissa represents the distance from the nozzle exit and the ordinate represents a non-dimensional time lag. Correlation peaks exist in $1 \leq x \leq 2.5$, with peak values at $x \sim 1.5$, which is the location where vortex intrusion is identified in figure 7(*a*). This indicates that vorticity fluctuations (due to vortex intrusion) at these spatial locations are closely associated with acoustic fluctuations in the downstream radiating direction. From the perspective of shear layer instability waves, this response to forcing can also be interpreted as the enhancement of the Kelvin–Helmholtz instability wave packet at the forcing frequency, resulting in increased downstream radiation (Cavalieri, Jordan & Lesshafft 2019).

The second stream of acoustic radiation seen in figure 6(*c,d*) is predominantly in the sideline direction ($70° \leq \theta \leq 90°$). This emerges from the nozzle exit and, therefore, is most likely a direct signature of the perturbations emitted from the plasma actuator. The behaviour of the first (downstream) acoustic stream is similar on both the principal axes, whereas the spatial form of the second (sideline) stream differs on these two planes. This reaffirms the hypothesis that the sideline band is a direct signature of actuation, which is more likely to be affected by the variations in actuator placement on the longer and
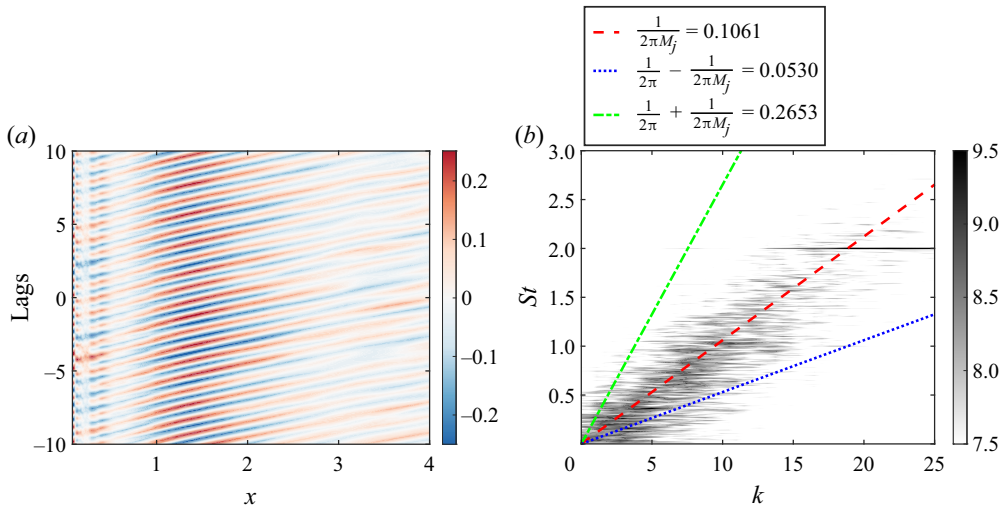
964 A11-12

Figure 8. (*a*) Cross-correlation contour for $St = 1$ forcing, and (*b*) wavenumber-frequency contour for $St = 2$ forcing.

shorter edges of the nozzle. Although not discernible from figure 6(*c*,*d*) due to its relatively low-amplitude sideline signature, the $St = 1$ forcing results in a feeble interference pattern between the above two streams.

A similar analysis on the baseline jet phase averaged with $St = 2$ as the reference signal indicates a negligible presence of high frequencies in the near field (figure 6*e*,*f*). The controlled jet, however, reveals a response pattern containing three dominant acoustic streams on the minor axis plane. The first has a predominantly downstream directivity pattern, with $\theta \leq 50°$, as seen in figure 7(*b*). This can be attributed to the supersonic convection of coherent vortical waves in the thin shear layer. To probe this further, we obtain the space–time Fourier-transformed vorticity fluctuations (ω'_z) along the nozzle lip line (represented by a dotted blue line in figure 7*b*). The wavenumber–frequency contour plot is shown in figure 8(*b*). The abscissa represents wavenumber (k), the ordinate represents frequency (St) and the contours correspond to the logarithm of energy. Only the regime of positive wavenumbers are shown, as the contribution to energy from upstream propagating waves is significantly lower than that of the downstream propagating waves. The ratio of the abscissa to ordinate yields the convective speed St/k, which is equivalent to $(1/2\pi)\omega/k$. The blue dotted line, red dashed line and green dashed-dot line on these contours represent phase speeds of $u - c$, c and $u + c$, respectively. Here, c is the speed of sound based on jet exit conditions and u is the jet exit velocity. Thus, any energy content to the left of the red dashed line has a locally supersonic convective speed and contributes towards acoustic emissions. In figure 8(*b*) almost half of the energetic spectral range appears in the supersonic regime. As suggested by the low wavenumbers, it is evident that coherent vortical structures travelling at locally supersonic convective speed are responsible for the emission of Mach waves in the downstream direction.

The second stream of acoustic waves in figure 6(*e*,*f*) is along the sideline direction, representative of the actuator signature, with much higher intensity than that observed for the $St = 1$ forcing. The asymmetry of this stream on the two planes can again be associated to the difference in the number actuators placed on the longer and shorter edges of the nozzle. The third stream with peak radiation along $\theta = 60°$ appears to be a

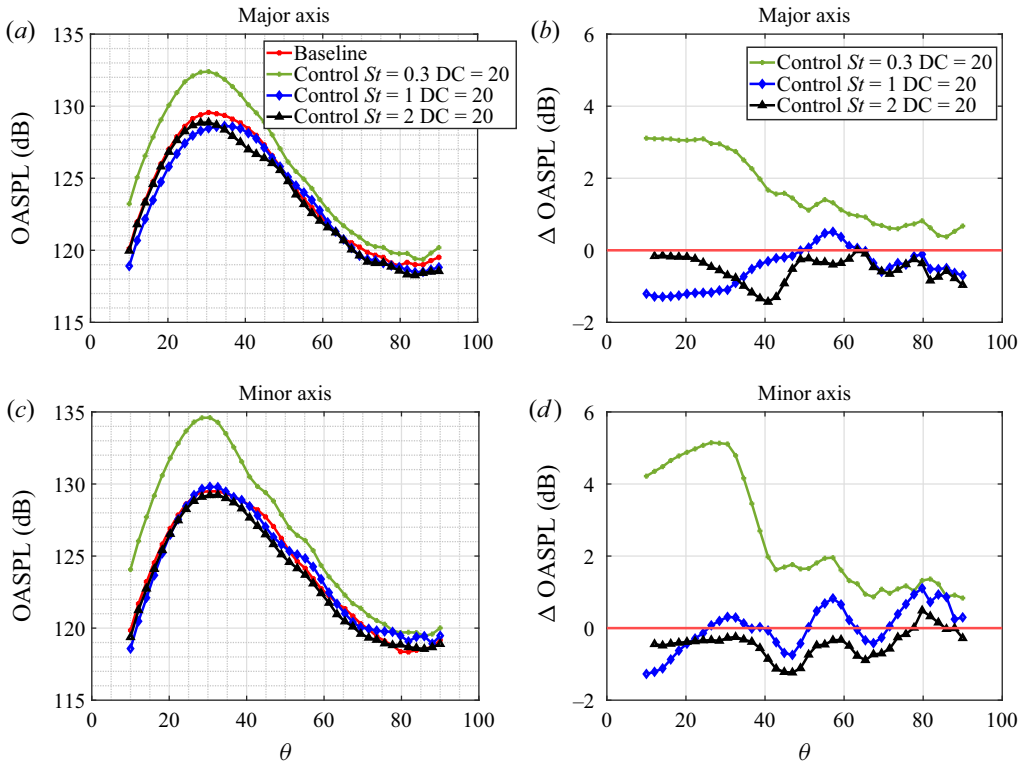**964** A11-13

Figure 9. Far-field OASPL comparison between the baseline jet and jets with control at various polar angles on (*a*) the major axis and (*c*) the minor axis plane. The OASPL difference between the baseline jet and jets with control at the same far-field locations on (*b*) the major axis and (*d*) the minor axis plane. Red horizontal lines in (*b,d*) indicate the 0 dB datum.

result of interaction between the downstream radiation and the sideline actuator signature. A similar three-stream pattern is seen on the major axis plane, albeit at lower amplitudes.

4.1.2. *Far-field impact*

The far-field acoustic impact of forcing is quantified in figure 9 by plotting the polar variation of far-field OASPLs on the two principal planes of the nozzle at $r = 40$. Figure 9(*a,c*) shows variation of the OASPL, and figure 9(*b,d*) shows the change in OASPL levels of the controlled jets in relation to the baseline jet. This is calculated using

$$\Delta\text{OASPL} = \text{OASPL}_{Controlled} - \text{OASPL}_{Baseline}. \tag{4.1}$$

Negative/positive values of ΔOASPL signify noise reduction/increase upon implementing control. The sound levels of the baseline jet are nearly identical on the major and minor axis planes, consistent with the azimuthally axisymmetric far-field acoustics seen in low-AR rectangular jets without flapping (Heeb *et al.* 2013; Viswanath *et al.* 2016; Chakrabarti *et al.* 2021). However, the impact of control is different on the two planes.

When the jet is forced at $St = 0.3$, the noise levels across polar angles increase significantly. The increase in peak noise levels is about 5 dB on the minor axis plane, and slightly over 3 dB on the major axis plane, as seen in the ΔOASPL levels. The acoustic asymmetry is more prominent at shallow polar angles, with the sideline angles indicating

964 A11-14

comparable ΔOASPL levels on both the planes. The asymmetry could be contributed by the inherent differences between the nature of coherent structures excited in the shear layers, as well as differences in the number of actuators between the shorter and longer edges of the nozzle. The nature of the excited shear layer structures on the two planes will be further explored in the following section using phase-averaged analysis. Recent linear analysis by Rodriguez, Prasad & Gaitonde (2021) has identified an elliptic nature to wave packets in rectangular jets. Upon excitation, energizing of these wave packets can also contribute to enhanced asymmetry in the associated radiation pattern. This asymmetric noise amplification is consistent with increased intensity of super-directive acoustic waves seen in the phase-averaged dilatation contours (figure 6*a*,*b*).

High-frequency forcing (at $St = 1$ and 2) causes the far-field OASPL to reduce at certain polar angles, typically $\theta \leq 40°$, as seen in figure 9. Noise attenuation is also different between the two planes, with maximum reduction obtained on the major axis plane. On the major axis plane, forcing at $St = 1$ provides ~1 dB reduction at angles of peak noise levels ($20° \leq \theta \leq 40°$). The sideline also shows reduced noise levels that is consistent with the observation that the phase-averaged acoustic radiation signature on the major axis plane is significantly weaker in relation to the minor axis plane (figure 6*c*,*d*). The effectiveness of $St = 1$ forcing on the minor axis plane is relatively weaker. While noise levels at very-low polar angles indicate reduction, the peak noise levels remain similar to that in the baseline jet. The increase in noise levels at $\theta > 70°$ results from the additional sideline radiation seen earlier in the phase-averaged contours.

Forcing at $St = 2$ also has different signatures on the two planes, but sound reduction achieved at peak noise polar angles is relatively smaller. On the minor axis plane, the peak reduction is at $\theta = 45°$. A lack of noise reduction along downstream angles, $\theta \leq 40°$, is attributed to the first stream of acoustic radiation seen earlier in figure 6(*f*). A similar loss in control effectiveness is observed at $\theta \sim 60°$, owing to the third stream of acoustic waves. The marginal noise increase at $\theta > 75°$ is due to the additional sideline radiation emerging as a result of actuation. Main differences on the major axis plane are that the peak noise reduction is higher (by ~0.5 dB), and the sideline noise also attenuates. Both these can be attributed to the fact that the acoustic waves from actuation on the major axis plane are of lower intensity than the minor axis plane.

The trends observed in ΔOASPL are further explored using the SPL spectra in figure 10. The SPL at $\theta = 34°$, corresponding to the polar angle of peak radiation, are shown in figure 10(*a*,*c*), for the major and minor axis planes, respectively. Corresponding SPL plots at $\theta = 80°$ (jet sideline) are shown in figure 10(*b*,*d*). Each plot contains the baseline and controlled jets. The actuator signature appears as sharp peaks at forcing frequencies in the spectra. A key observation is that the actuator signature is much stronger (higher amplitude peaks) on the minor axis plane than on the major axis plane, consistent with the observations made in near-field phase-averaged contours.

Forcing at $St = 0.3$ generates the most dominant peak over the broadband hump (of the baseline), with a magnitude that is 3 to 5 dB higher, contributing to the increased OASPL seen earlier in figure 9. The jet sideline, however, does not experience such a drastic increase in sound levels, confirming the observation that the impact of $St = 0.3$ forcing is primarily to increase the super-directive radiation. These observations regarding the sideline also match with experimental results by Samimy *et al.* (2009) for LAFPA-controlled circular jets, where OASPL in the sideline did not show any appreciable change.

Forcing at $St = 1$ decreases the radiated energy, particularly at low- and mid-band frequencies in comparison to the baseline case. The encouraging observation is that, at
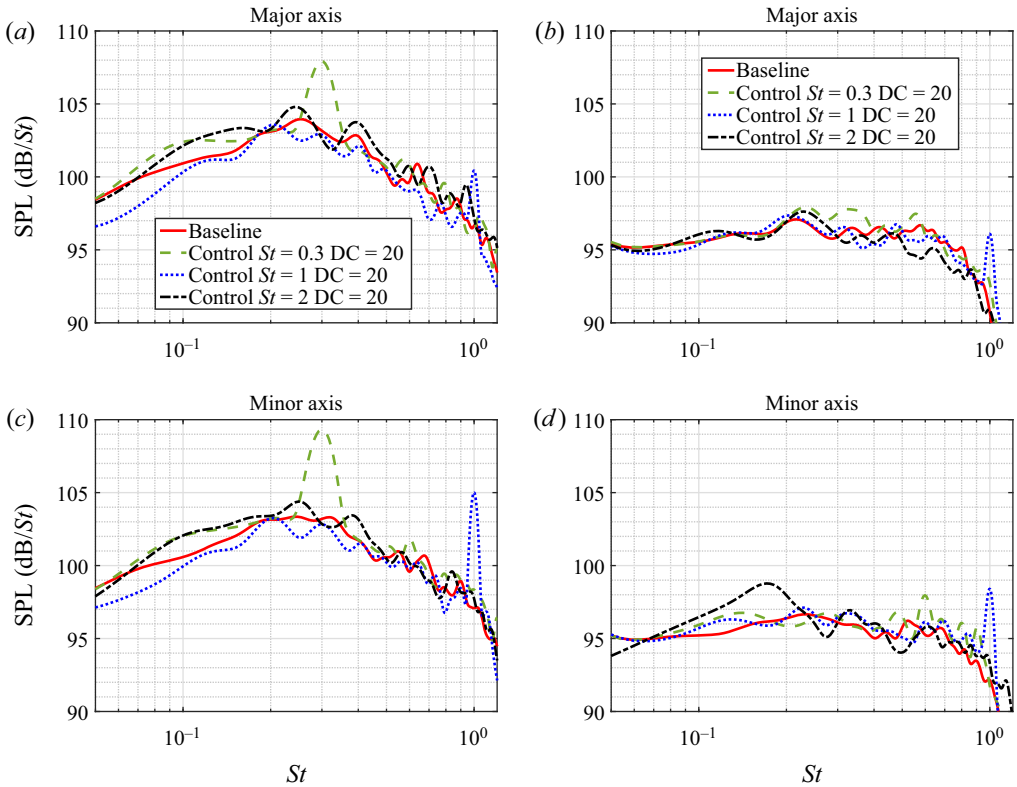
Figure 10. Effects of forcing frequency on far-field SPL: comparison of results form the baseline jet and jets with control at a peak noise radiating angle of $\theta = 34°$ on (*a*) the major axis and (*c*) the minor axis. Plots (*b,d*) are corresponding results at a jet sideline angle of $\theta = 80°$.

peak radiating angles, energy within the broadband hump ($0.2 \leq St \leq 0.4$) corresponding to the jet column mode is reduced. For peak radiating angles, the actuator signature is much smaller on the major axis plane, with a magnitude lower than the broadband noise hump. This explains the higher levels of noise attenuation on the major axis plane (figure 9). Along the jet sideline, forcing at $St = 1$ induces very little variations in the energy content at most frequencies. This coupled with the additional signature of the actuators result in an increase in sideline OASPL.

Forcing at $St = 2$ has minimal favourable impact on the radiated energy, with noise reduction limited to higher frequencies ($St > 0.6$). However, $St = 2$ has a relatively weaker far-field actuator signature compared with the other cases.

A similar trend of noise reduction was observed with a higher duty cycle of 50 %, with forcing frequencies of $St = 1$ and $St = 2$. In summary, among the various frequencies of actuation studied, $St = 1$ forcing yields a good balance between reduced overall sound levels and moderate increase in sideline noise levels on some nozzle planes. This must also be interpreted in the context that the sideline noise levels are much lower (by $\sim$12 dB) than the peak noise levels.

4.2. *Effect of duty cycle*

Since forcing at $St = 1$ was observed to be the most effective in the previous analysis, we report the impact of the duty cycle at this frequency. Studies by Speth & Gaitonde (2013)
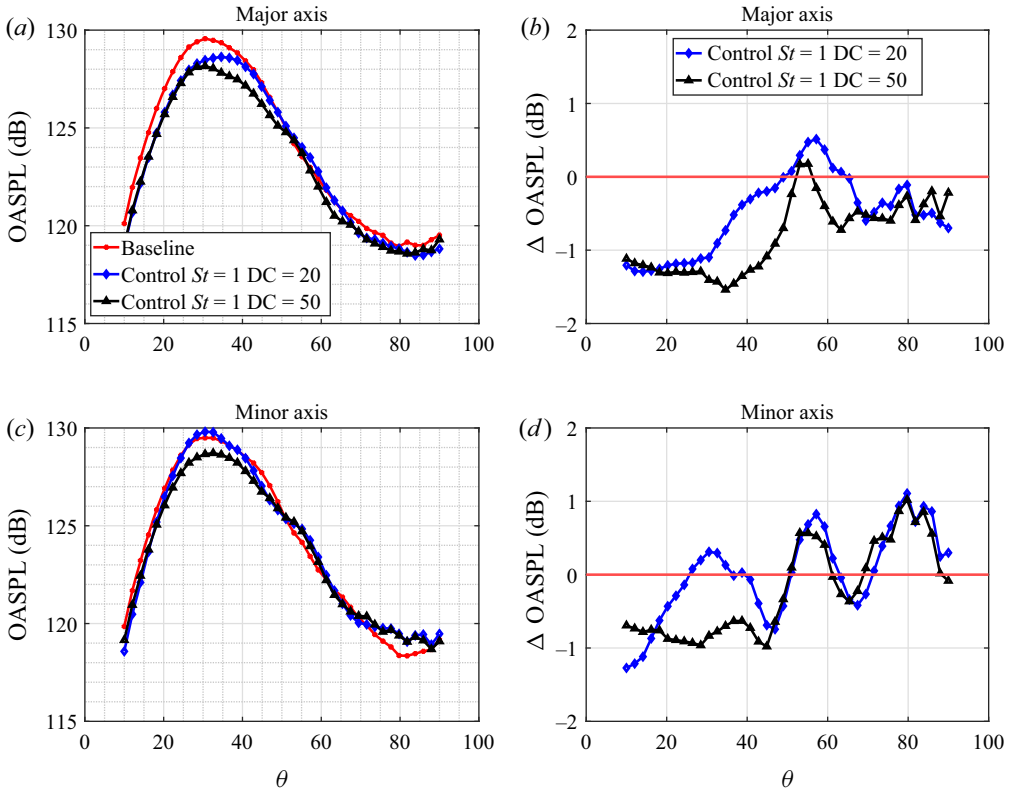
964 A11-16

Figure 11. Effects of duty cycle on far-field noise: far-field OASPL comparison between the baseline jet and jets with $St = 1$ DC20/DC50 control at various polar angles on (a) the major axis and (c) the minor axis plane. Corresponding OASPL differences between controlled jets and the baseline jet on (b) the major axis and (d) the minor axis plane. Red horizontal lines in (b,d) indicate the 0 dB datum.

on circular jets showed that while the plume response was sensitive to lower duty cycles, higher duty cycles typically above 50 % showed very similar mean flow and fluctuation statistics. They also reported that a jet forced at a 100 % duty cycle had a behaviour that closely resembled an uncontrolled jet. Based on these observations, the present study is limited to two duty cycles, 20 % and 50 %. The results are presented in figure 11 for DC20 and DC50. Figure 11(a,c) shows the far-field OASPL comparison among the baseline and the two controlled jets on the major and minor axis planes, respectively. Figure 11(b,d) shows the corresponding ΔOASPL.

Comparing figures 11(b) and 11(d), the major axis shows higher levels of noise attenuation for both duty cycles. Although both DC20 and DC50 attain ~1.3 dB reduction for shallow angles ($10° \leq \theta \leq 30°$), the latter outperforms along peak noise angles corresponding to $\theta \sim 35°$. This is evident in figure 11(b), where the maximum reduction is obtained as 1.6 dB for DC50. The higher duty cycle also reduces the ΔOASPL overshoot at $\theta \sim 55°$, further improving the overall performance. Although not as effective as on the major axis plane, DC50 still performs better than DC20 on the minor axis plane. As opposed to the major axis trends, the noise in the controlled jets increases along the sideline ($\theta > 75°$) on the minor axis plane, due to the direct response to the forcing frequency, which causes increased sideline radiation as discussed in the previous section.
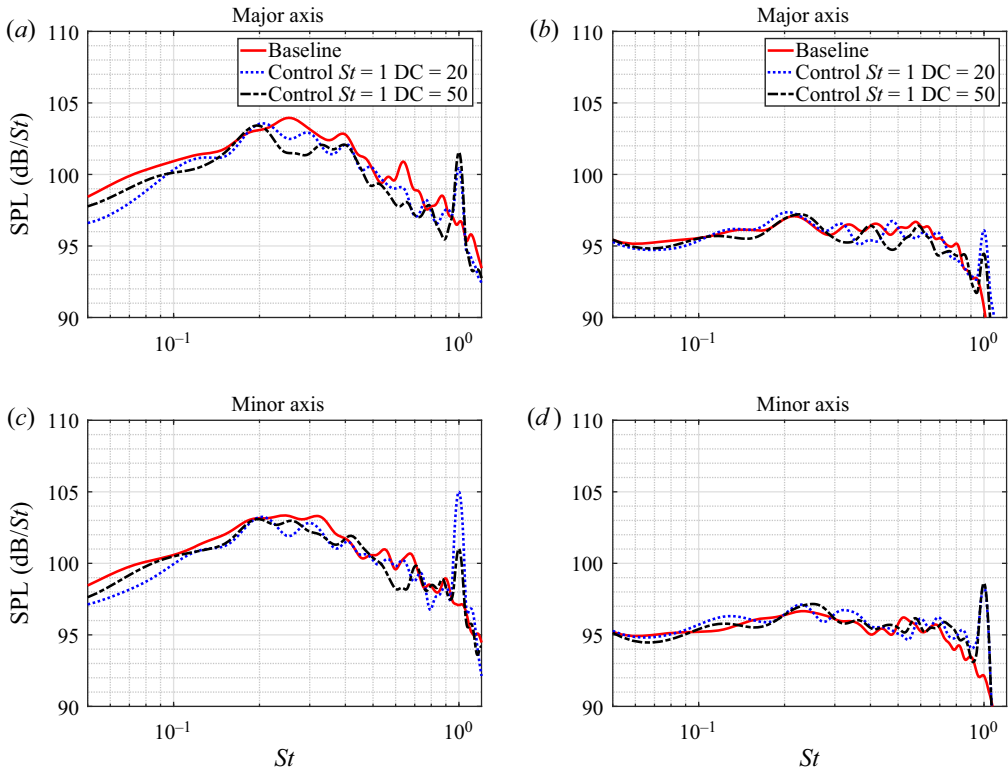
Figure 12. Effects of duty cycle on far-field noise: far-field SPL comparison between the baseline jet and jets with control at a peak noise radiating angle of $\theta = 34°$ on (*a*) the major axis and (*c*) the minor axis. Plots (*b*,*d*) are the corresponding results at a jet sideline angle of $\theta = 80°$.

Figure 12 shows the SPL spectra comparison among the baseline and controlled cases. The left and right columns correspond to $\theta = 34°$ and $\theta = 80°$, respectively. The top and bottom rows correspond to major and minor axis planes, respectively. The improved performance of DC50 on the major axis plane is due to the SPL reduction near the column mode frequency, $0.2 \leq St \leq 0.4$, and higher frequencies, $0.6 \leq St \leq 0.7$. This, along with the relatively weaker actuation signature facilitates the 1.6 dB reduction in overall noise levels seen earlier in figure 11(*b*). A similar reduction in SPL is seen on the minor axis plane as well in figure 12(*c*), but the reduction at column mode frequency is not as much as that seen on the major axis plane. On both the major and minor axis planes, neither duty cycles impact the sideline spectra significantly, as seen in figure 12(*b*,*d*). Therefore, the emergence of the actuator tone effectively increases the OASPL.

The foregoing analyses confirm that the forcing at $St = 1$ with a 50 % duty cycle provides the most reduction in far-field sound, within the parameter space tested. They also highlight the fact that the choice of forcing frequency plays a crucial role in altering noise characteristics of the jet, due to its manipulation of shear layer instabilities and evolution of coherent structures. The duty cycle seems to provide a secondary effect by reinforcing this response. As highlighted in § 1, a key focus of this study is to identify causal mechanisms in the plume that directly result in the observed acoustic trends. To this end, the following sections will first explore in detail the shear layer dynamics and radiating characteristics of key controlled cases. This will be followed by evaluation of first- and second-order turbulent statistics of these jets.

964 A11-18

5. Response of the plume to actuation

Dynamics of the forcing frequency in the plume has a major impact on the resulting spatiotemporal scales in the controlled jets. While coherent turbulent features in the response may be highlighted through a vortex-identification technique, its acoustic impact can be identified using a suitable physical filtering strategy (Tinney & Jordan 2008; Unnikrishnan & Gaitonde 2016). These will be utilized below in conjunction with the phase-averaged flow field to study the controlled jets.

5.1. *Shear layer response*

The response of the shear layer to actuation is evaluated in figure 13(a–c) for $St = 0.3$, $St = 1$ and $St = 2$ forcings, respectively, at a 50 % duty cycle, using a phase-averaged Q criterion ($\tilde{Q}$), coloured with phase-averaged streamwise velocity ($\tilde{u}$). The four snapshots, figure 13(a–d), correspond to the states at four representative time instances within the phase-averaged cycle, $0 \leq \tilde{t} \leq T_f$, in terms of the percentage of $\tilde{t}/T_f$. The time period of forcing, T_f, is defined as $1/St_f$, where St_f is the non-dimensional frequency of forcing. To highlight the vortical dynamics, figure 13 identifies two flow structures, A1 and B1, at the beginning of the phase-averaged cycle in each case. Here A1 corresponds to the features that are generated when the actuators turn off, and eventually develop into lambda vortices; B1 is an elongated vortical element parallel to the shear layer, that is generated when the actuators turn on, at the beginning of a cycle. In each frame, the upper and lower arrows track A1 and B1, respectively.

With $St = 0.3$ forcing (figure 13a), A1 and B1 flow structures convect downstream and the 'legs' of the A1 lambda vortices are stretched in the high-speed core, while the 'head' region lags in the ambient fluid as seen in figure 13(a-ii). Interaction of A1 with B1 vortical structures causes the head region to be pinched off, as seen in figure 13(a-iii,iv). The pinched head regions develop into a larger set of lambda vortices as shown by the dashed circle in figure 13(a-i). These vortices eventually coalesce to form a single lambda vortex that convects downstream as demarcated by the dashed circle in figure 13(a-ii,iii). This shows that the shear layer responds to the forcing at $St = 0.3$ by generating large coherent vortical structures, at the scales of the plume, resulting in increased far-field noise levels.

For $St = 1$ forcing, the initial development of A1 and B1 structures follow a similar pattern. The 'legs' of the A1 lambda vortices are stretched in the high-speed core, while the 'head' region lags in the ambient fluid, resulting in the head region being pinched-off from the vortical structure, as seen in figure 13(b-ii). However, further evolution of these vortical structures differ from the $St = 0.3$ forcing. In figure 13(b-iii) the pinched head regions interact with the trailing vortical element, B1, and creates an 'azimuthally' connected vortical element. This results in a staggered pattern of lambda vortices in B1, relative to A1, evident in figure 13(b-iv). Comparing the velocity contours on A1 and B1 in figure 13(b-iv), B1 lambda vortices exist in the inner shear layer. Around $x \sim 2.5$ downstream of the nozzle exit, these structures disintegrate. Thus, $St = 1$ forcing generates a flow response at the scales of the shear layer thickness, including streamwise vortices in the shear layer, generally considered favourable to reducing coherent sound generation mechanisms.

A similar analysis for $St = 2$ forcing is shown in figure 13(c). The B1 vortex element initially parallel to the shear layer disintegrates downstream as seen in figure 13(c-ii), and merges with A1 to form a single row of lambda vortices. While the 'head' regions of this row of lambda vortices are formed by the A1 row of vortices present in the (low-speed) outer shear layer, the 'legs' are formed by the stretched B1 row of vortices that reside
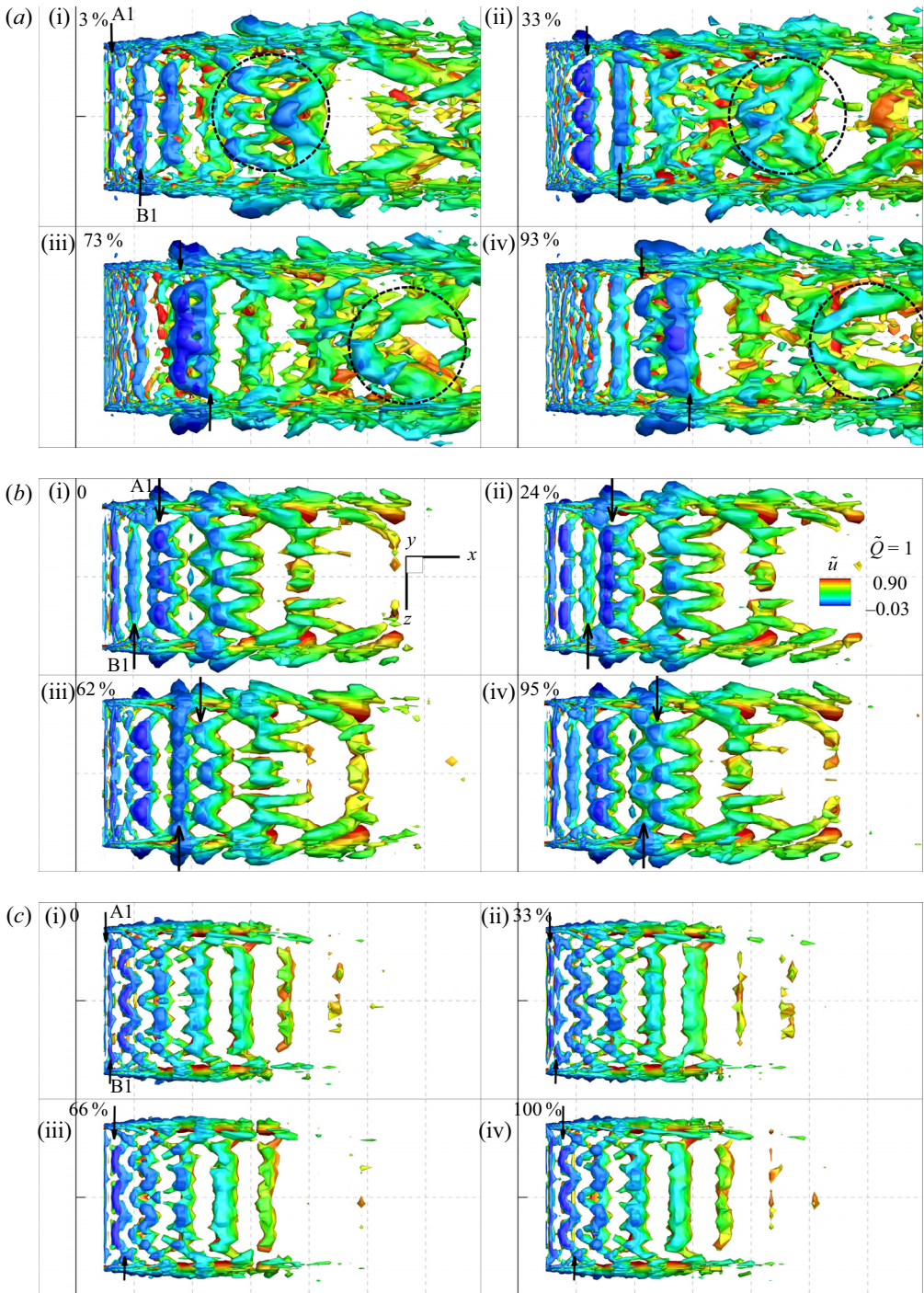
Figure 13. Phase-averaged flow fields for (*a*) $St = 0.3$ (DC20), (*b*) $St = 1$ (DC50) and (*c*) $St = 2$ (DC50) forcing, at the indicated phase percentages. The top (B1) and bottom (A1) pointing arrows track the evolution of structures generated when the actuator is switched on and off, respectively. Distance between two vertical grid lines is $0.5D_{eq}$.
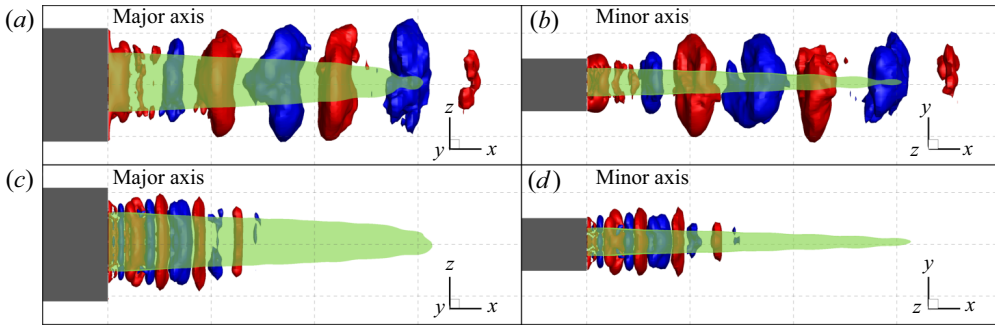
Figure 14. Instantaneous isolevels of phase-averaged acoustic fluctuations at $A_x = \pm 0.003$ for $St = 0.3$ DC20 forcing, projected onto (*a*) the major axis plane and (*b*) the minor axis plane. Plots (*c,d*) are corresponding results for the $St = 1$ DC50 forcing. The potential core is shown using and isolevel at $u = 0.9$. The distance between consecutive vertical and horizontal grid lines are $2D_{eq}$ and $1D_{eq}$, respectively.

within the (high-speed) inner shear layer. These vortex rings are sustained to about $x \sim 1.5$ from the nozzle exit, after which they disintegrate. Unlike $St = 1$ forcing, due to the rapid decay rate over a very small streamwise extent, and smaller spatial scales being impacted, $St = 2$ forcing does not efficiently manipulate the energy-containing scales in the shear layer and, thus, only minimally affects the acoustic emissions.

5.2. *Acoustic response of the plume*

In the turbulent plume the fluctuations are dominated by the hydrodynamic content. Therefore, to understand the origin of the far-field noise signature of the controlled jets, we first isolate the acoustically relevant fluctuations in the plume using the following momentum potential theory (Doak 1989):

$$\rho \boldsymbol{u} = \bar{\boldsymbol{B}} + \boldsymbol{B}' - \boldsymbol{\nabla}(\psi_a' + \psi_T'). \tag{5.1}$$

This is achieved by performing a Helmholtz decomposition of the mass flux. Here, $\bar{B}$ and B' are the mean and fluctuating solenoidal components, respectively. The irrotational scalar potentials account for the acoustic (ψ_a') and thermal (ψ_T') components. Upon substituting the above relation in the continuity equation, we obtain two Poisson equations, which can be solved to extract the acoustic and thermal components in the jet, i.e.

$$\nabla^2 \psi_a = \frac{1}{c^2} \frac{\partial p}{\partial t}, \quad \nabla^2 \psi_T = \frac{\partial \rho}{\partial S} \frac{\partial S}{\partial t}. \tag{5.2a,b}$$

Here c is the local speed of sound and S is entropy. More details on the decomposition and its implementation can be found in Unnikrishnan & Gaitonde (2016). The following discussion will focus on trends in the streamwise acoustic fluctuations, $(-\partial \psi_a'/\partial x)$, due to its most influential role in defining the radiated noise in the downstream direction. It will be henceforth referred to as A_x for notational convenience.

The effect of actuation on the acoustic component is first isolated from the phase locked averaging as specified in § 4.1. Figure 14 shows an instantaneous snapshot of phase-averaged acoustic fluctuations, A_x. The figure shows a plane projected view of the isolevels of $A_x = \pm 0.003$ for $St = 0.3$, DC20 forcing (figure 14*a,b*) and $St = 1$, DC50 forcing (figure 14*c,d*).

In case of $St = 0.3$ forcing the acoustic response is amplified into a mostly axisymmetric large-scale wave packet that extends beyond the potential core of the jet. This is due to the jet resonating at the column mode, thus developing a global response at the forcing frequency. As expected in radiatively efficient wave packets, the length scales of these features are significantly higher than the local turbulent scales (Cavalieri *et al.* 2012). The response to $St = 1$ forcing is an axially compact wave packet, largely limited to the vicinity of the nozzle. It exhibits a strong influence of the rectangular nozzle geometry, due to the non-axisymmetric nature of the mean flow. The direct spectral impact of the high-frequency actuation is thus local in nature, and mostly appears in the sideline direction.

6. Impact on radiating characteristics

From the previous analyses, it is evident that the acoustic response in the plume and its far-field signature are sensitive to control parameters. Here we examine three main characteristics of the acoustic gain of the jet, which helps us explain the observed noise signatures. Those include the convective speed of the acoustic wave packet (Tam & Morris 1980; Tam & Burton 1984*a*,*b*), its azimuthal coherence (Sinha *et al.* 2014; Chakrabarti *et al.* 2021) and intermittency of dominant acoustic events (Kearney-Fischer, Sinha & Samimy 2013; Koenig *et al.* 2013). For brevity, this analysis is limited to the baseline jet and the controlled jet, $St = 1$, DC50, in which the control was most effective in achieving noise reduction.

6.1. *Convective speed*

The convective speed is quantified using wavenumber–frequency analysis in figure 15. These plots are obtained using spatiotemporal Fourier-transformed signals of A_x along a horizontal line at $r = 2.5$ from the jet centreline on the two principal planes. Here k and St represent streamwise wavenumber and frequency, respectively. Figure 15(*a*,*b*) shows the results for the baseline jet on the two principal planes. Corresponding results for $St = 1$, DC50 are provided in figure 15(*c*,*d*). Again, the blue dotted, red dashed and green dash-dot lines represent the slow-acoustic, sonic and fast-acoustic speed estimates, respectively, as detailed earlier in the context of figure 8(*b*). It has to be noted that this analysis is performed on the filtered acoustic component in the near field that exhibits a wave packet form (Chakrabarti *et al.* 2021), and precludes the contribution from the largely convective pseudo-sound or hydrodynamic pressure fluctuations (Unnikrishnan & Gaitonde 2016).

The acoustic wave packet in this supersonic jet has peak energy propagating at an average velocity of approximately $0.70U_j$, which is close to the jet exit sonic speed. Here c_j represents a reasonable approximation of the local sonic speed in the plume, since the jet is unheated. The baseline jet exhibits strong energy peaks within $0.1 \leq St \leq 0.5$ on both the major and minor axis planes. The radiating zone contains negligible energy below $St \sim 0.1$. In the vicinity of the column mode at $St \sim 0.3$, most of the energy in the acoustic wave packet is in the radiating zone, and the relative percentage of radiated energy for a given St increases with frequency. The energy levels, however, attenuate rapidly above $St \sim 0.6$, thus reducing the contribution of higher frequencies to the radiated noise. Thus, frequencies corresponding to the jet column mode possess relatively higher energy magnitudes in the supersonic radiating regime. This behaviour matches the observations seen in the far field, where noise spectra contain a broadband peak around $St \sim 0.3$ and roll off towards higher frequencies.
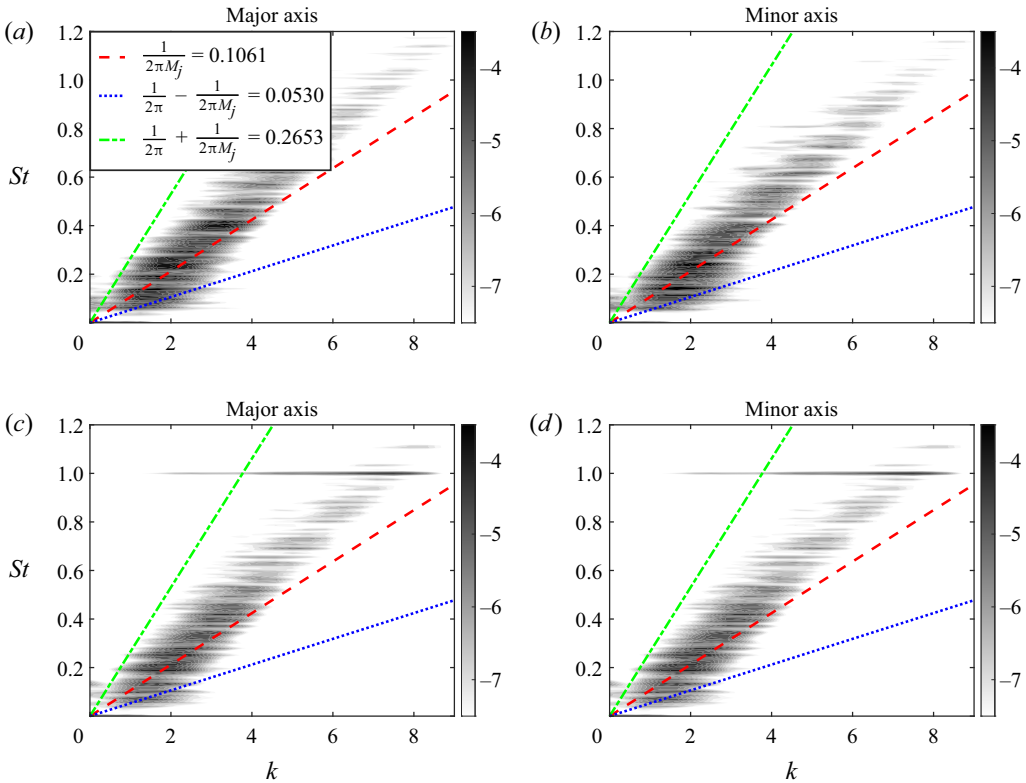
Figure 15. Wavenumber-frequency spectra of acoustic fluctuations in the baseline jet on (*a*) the major axis and (*b*) the minor axis plane. Plots (*c*,*d*) are the corresponding results for the jet with $St = 1$ DC50 forcing.

The jet controlled using $St = 1$, DC50 has attenuated energy content in the supersonic radiating band in the vicinity of the column mode, as seen in figure 15(*c*,*d*). Specifically, radiated energy at low frequencies below $St \sim 0.4$ reduces on both planes. It also contains a harmonic tone at the forcing frequency in the radiating zone. Energy content in the vicinity of the forcing frequency ($0.8 < St < 1$) also reduces in the controlled jet. This behaviour suggests that control has resulted in an energy redistribution from the lower frequencies and side-band frequencies, to the forcing frequency.

To further quantify the above trends, we compare the convective speeds of energy at two frequencies, representative of the dominant downstream noise radiation. These plots are shown in figure 16, where the abscissa indicates the phase speed and the ordinate shows the logarithm of power spectral density. Lines corresponding to key phase speed values are also shown. The solid vertical line corresponds to c, the dotted line corresponds to $u - c$, the dashed-dot line shows u and the dashed line represents $u + c$. Plots are shown for two frequencies, $St = 0.5$ (figure 16*a*) and $St = 0.3$ (figure 16*b*). Results for both the baseline (solid line) and controlled jet (dashed line) on the major (red) and minor (blue) axis planes are included. Energy content to the right of the black solid line has a supersonic convective speed and contributes to acoustic radiation as indicated by the arrow.

Comparing the two solid lines for $St = 0.5$ in figure 16(*a*), it is evident that there is a slight acoustic asymmetry in the near field of the baseline jet, with higher energy levels on the major axis plane than the minor axis plane. This is an effect of the nozzle AR, which causes the sampling locations to be closer to the jet on the major axis plane than on the
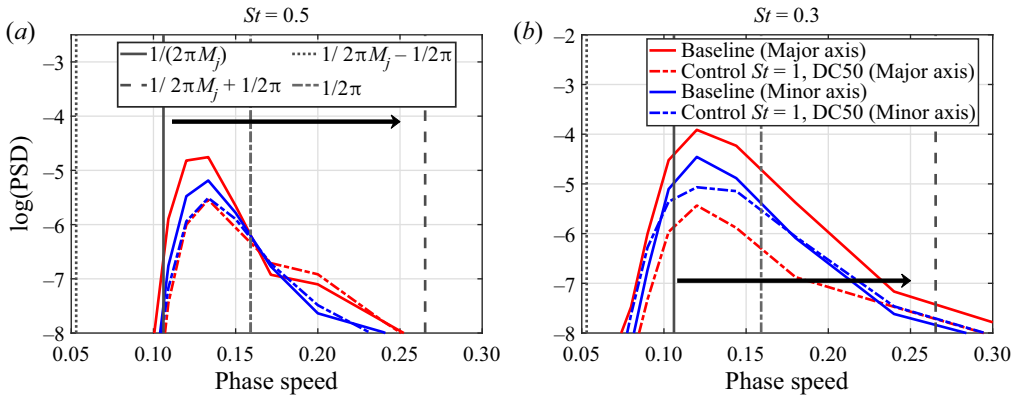
Figure 16. Distribution of the power spectral density with respect to phase speed at (*a*) $St = 0.5$ and (*b*) $St = 0.3$.

Number of snapshots	Sampling frequency (St)	Window	Overlap	Number of blocks (n_{blk})	Number of frequencies (n_{fft})
2000	10	256	50 %	14	256

Table 2. Parameters used for SPOD.

minor axis plane. Between the baseline and controlled cases, there is a clear reduction in energy in regions to the right of the solid black line in the latter, indicative of reduction in the radiating acoustic component at this frequency. This reduction seen at $St = 0.5$ is close to one order of magnitude, and the controlled jet exhibits an almost identical noise signature on both principal planes at this frequency. The energy levels at $St = 0.3$ (shown in figure 16*b*) in the baseline jet is the highest, as expected from a perfectly expanded jet. The energy reduction at $St = 0.3$ on the major axis is substantially greater than that at other frequencies, particularly when compared with that achieved on the minor axis plane. This near-field asymmetric effect of control is recreated as far-field SPL trends in a consistent manner, as seen earlier in figure 12. It must be noted that while the effect of control reduces the magnitude of energy at supersonic phase speeds, the peak energy in the baseline and controlled jets is still observed at similar phase speeds.

6.2. *Azimuthal coherence*

To identify how the control has modified the dominant spatial scales in the acoustic wave packet and its azimuthal coherence at radiating frequencies, we perform spectral proper orthogonal decomposition (SPOD) (Towne, Schmidt & Colonius 2018; Schmidt & Colonius 2020) of the acoustic mode, A_x, within a subdomain spanning $0 \leq x \leq 15$, $-2 \leq y \leq 2$ and $-2 \leq z \leq 2$. Parameters used for the decomposition are listed in table 2.

Figure 17 compares the eigenvalue spectra for the baseline jet (solid line) and the jet with $St = 1$, DC50 forcing (dashed line). Plots for the first three dominant modes for both cases are shown. Spectra of the baseline case show similar behaviour to that seen in the far-field SPL (see figure 10). A broadband peak exists between $0.15 \leq St \leq 0.4$, and peak eigenvalue magnitudes are observed at $St \sim 0.3$, consistent with the findings from the frequency–wavenumber spectra and the far-field noise spectra. A significant gap exists
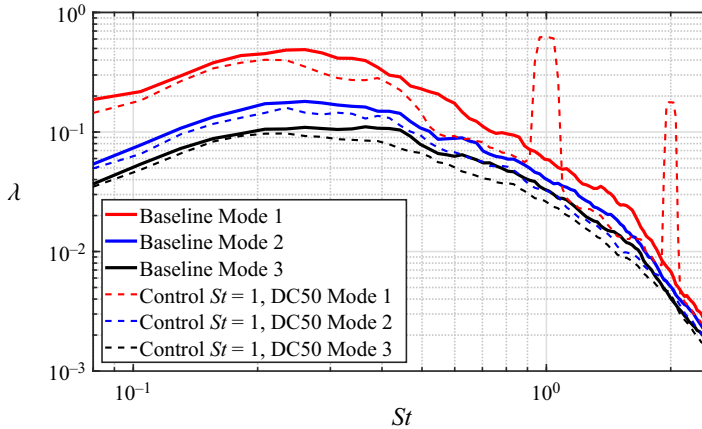
964 A11-24

Figure 17. Eigenvalue spectra of acoustic fluctuations from spectral proper orthogonal decomposition.

between mode 1 and mode 2 of the baseline jet at frequencies up to $St \sim 0.9$, suggesting that the acoustic component of the baseline jet has a low rank nature at frequencies of interest. The phase speed distribution of energy in the source data and the SPOD mode 1 displayed similar shapes at these frequencies, consistent with this low rank behaviour. The low rank behaviour is relatively negligible at higher frequencies, above $St \sim 1$.

The eigenvalues across most of the frequencies are smaller in the controlled jet in the leading mode, indicative of a broadband energy reduction in the acoustic component. More importantly, peak energy reduction occurs around $St \sim 0.3$ and between $0.6 \leq St \leq 0.9$, corresponding to the column mode frequency and the radiating spectral range. Two dominant peaks are seen at $St = 1$ and $St = 2$, resulting from the actuation frequency and its first super harmonic being generated through nonlinear interactions in the flow. The spectral shapes of subsequent modes (modes 2 and 3) are similar to the baseline jet, albeit at slightly lower values, and has a minimal direct signature of the actuation frequency. Another key observation is that the rank gap near the column mode is reduced in the controlled jet. This reduction is seen predominantly between $0.2 \leq St \leq 0.4$ with a maximum reduction of about 48 % at $St \sim 0.33$. The above estimate is based on the difference between the eigenvalues of the first and second modes for a given frequency. This suggests that the control is capable of redistributing energy within a wider range of scales, thus limiting instances of large-scale radiation events often associated with coherent structures.

To understand the changes effected in the coherent structures by control, the spatial support of the leading two SPOD modes at $St = 0.3$ are reported in figure 18. Figure 18(*a,b*) corresponds to the baseline and control with $St = 1$, DC50 forcing, respectively. While the first column of images shows the isolevels of the SPOD modes, the subsequent columns show the first three modes obtained from an azimuthal Fourier decomposition of the respective SPOD modes. This decomposition is carried out using the following formulation:

$$q(x, r, \phi) = q_a^0(x, r) + \sum_{m=1}^{\infty} q_a^m(x, r) \cos(m\phi) + q_b^m(x, r) \sin(m\phi). \qquad (6.1)$$

Here m refers to the azimuthal mode number and $q_a^m(x, r)$ and $q_b^m(x, r)$ are the azimuthally invariant spatial supports determined by

$$q_a^0(x, r) = \frac{1}{2\pi} \int_{-\pi}^{\pi} q(x, r, \phi) \, \mathrm{d}\phi, \qquad (6.2)$$

$$q_a^m(x, r) = \frac{1}{\pi} \int_{-\pi}^{\pi} q(x, r, \phi) \cos(m\phi) \, \mathrm{d}\phi, \qquad (6.3)$$

$$q_b^m(x, r) = \frac{1}{\pi} \int_{-\pi}^{\pi} q(x, r, \phi) \sin(m\phi) \, \mathrm{d}\phi. \qquad (6.4)$$

Additional details about the decomposition can be found in Chakrabarti *et al.* (2021). The azimuthal origin ($\phi = 0$) is set at the minor axis plane of the jet (positive y axis). The isolevel for a given azimuthal mode is chosen to qualitatively represent its spatial extent. For ease of quantitative comparisons, inset images with contours of $\sqrt{(q_a^m)^2 + (q_b^m)^2}$ for the corresponding azimuthal modes are also shown. In the following discussion the term mode/modes will be used to reference a SPOD mode (column 1), while the term ϕ mode will be used in reference to the azimuthal mode obtained from Fourier decomposition.

The coherent acoustic component of the baseline jet as obtained from the leading SPOD modes 1 and 2 (figure 18*a*) is dominated by azimuthally axisymmetric structures. This is further established by the relative amplitudes of the azimuthally decomposed ϕ modes. The spatially localized growth and decay of the acoustic component is consistent with observations on energetic structures made by Arndt, Long & Glauser (1997) and Colonius & Freund (2002) for circular jets, Chakrabarti *et al.* (2021) and Lakshmi Narasimha Prasad & Unnikrishnan (2023) for rectangular jets and Lakshmi Narasimha Prasad *et al.* (2022*a*) for diamond jets. Due to the relatively low AR of the current configuration, most of the energy is present in the axisymmetric ϕ mode 0. This is evident by comparing amplitudes of $\sqrt{q_a^2 + q_b^2}$ in the inset contours. Here ϕ mode 1 and ϕ mode 2 represent single and double helical structures, respectively, and suggest a depreciating spatial support at increasingly higher ϕ modes. The higher helical modes are primarily present along the corners. In mode 2 of the baseline jet, the higher ϕ modes are relatively stronger than those in mode 1, since energetically subdominant structures are responsible for deviation from an axisymmetric nature.

Upon implementing LAFPA-based control, the non-axisymmetric helical ϕ modes are enhanced, as seen in figure 18(*b*). Mode 1 and its ϕ modes indicate that the axisymmetric mode still remains the most energetic, like in the baseline jet. However, the formation of localized shear layer vortices downstream of the actuators modify the acoustic response, and ϕ mode 1 becomes more pronounced compared with the baseline jet. This behaviour is more obvious in mode 2 of the controlled jet where ϕ mode 0 shows very little spatial support at locations between the nozzle exit and core collapse location. Within this region, the spatial support of ϕ mode 1 significantly increases, resulting in a dominant single helical structure. This is also seen in the magnitude contours below the ϕ modes, which indicate higher intensities at locations between the nozzle exit and core collapse location. Studies by Michalke & Fuchs (1975) have established that lower/higher azimuthal modes have higher/lower downstream radiative efficiency. As shown above, the LAFPA actuation enhances azimuthal percolation of energy within the dominant acoustic modes, further
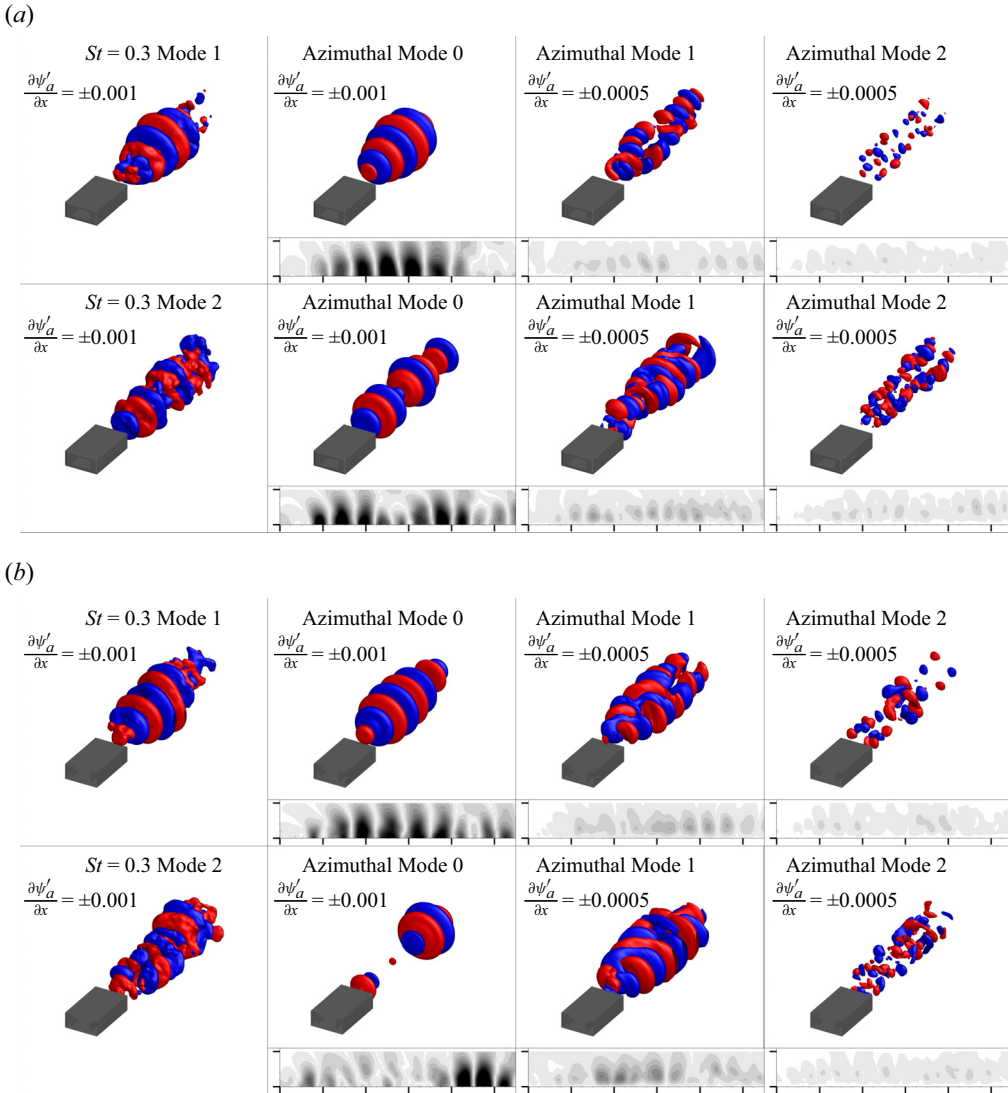
(*a*)

(*b*)

Figure 18. (*a*) Isolevels of the leading two SPOD modes of acoustic fluctuations in the baseline jet at a frequency of $St = 0.3$, and its azimuthally decomposed Fourier modes. The first column shows the SPOD modes, while the subsequent columns show the corresponding three azimuthal Fourier modes. Here, (*b*) shows the same results for the $St = 1$, DC50 controlled jet. Inset figures below each azimuthal mode show contours of the corresponding spatial coefficients, $\sqrt{q_a^2 + q_b^2}$. Spatial extent of the contour plots is $0 \leq x \leq 11$, and $0 \leq r \leq 2$. The ticks on the contour plot axes are spaced at $2D_{eq}$. Contour levels are uniformly distributed from 0.0001 to 0.005.

explaining the observation that the controlled jet exhibits lower SPL in the far field, near the column mode.

6.3. *Intermittency*

We now evaluate the intermittent nature of the radiated acoustic component, due to its influential role in deciding far-field OASPL (Crawley & Samimy 2014). For this, the
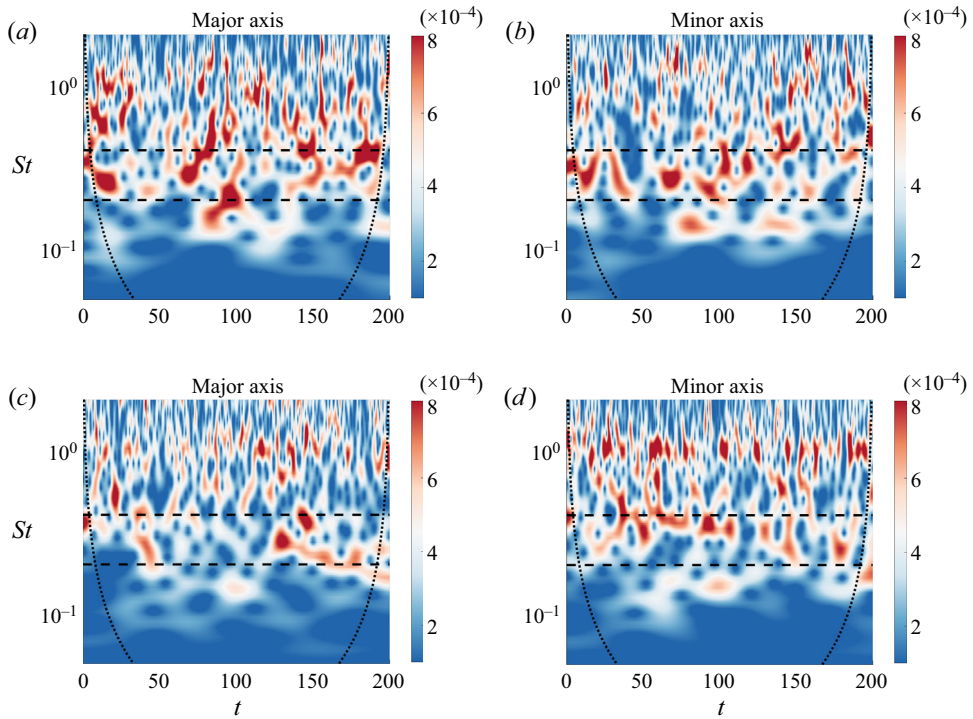
Figure 19. Scalograms of the acoustic fluctuations at $r = 2.5$, $\theta \sim 32°$ for the baseline jet on the (*a*) the major axis and (*b*) the minor axis plane. Plots (*c*,*d*) are corresponding results for the jet with $St = 1$ DC50 forcing. Dotted black curves demarcate the cone of influence, while the horizontal dashed black lines highlight the frequency band of interest.

time-frequency characteristics of A_x are obtained using a Morse wavelet transform (Lilly & Olhede 2009, 2012). The data are sampled at $\theta \sim 32°$, at $r = 2.5$ on the major and minor axis planes. The resulting scalograms for the baseline and controlled ($St = 1$, DC50) cases on the major and minor axis planes are shown in figure 19. The dotted lines demarcate the cone of influence, which segregates the region of accuracy (inside the cone) from the potentially erroneous region, affected by wavelets stretching beyond the edges of observation interval (outside the cone). Previous analyses identified energy peaks within $0.2 \leq St \leq 0.4$ in the baseline jet as the prime contributors to the peak noise signature, and are therefore chosen as the frequency band of interest. This is highlighted between black dashed lines on the scalograms.

The baseline jet exhibits strong intermittent acoustic events on both the major and minor axis planes within the frequency band of interest, as seen in figure 19(*a*,*b*). They are known to cause intermittent packets of sound radiation in the far field (Unnikrishnan & Gaitonde 2016). Application of control reduces the intensity of these intermittent events in figure 19(*c*,*d*). This effect is much more pronounced on the major axis plane in comparison to the minor axis plane. Regions around $St = 1$ show increased activity, as a result of actuation, which is more prominent on the minor axis plane.

To quantify the reduction of intermittent extreme acoustic events in the controlled jet, histograms are obtained in figure 20. Abscissa denotes the scalogram magnitude (cwt) obtained from performing the wavelet transform while the ordinate represents the ratio of the number of occurrences in a given bin to the total number of occurrences. They show the
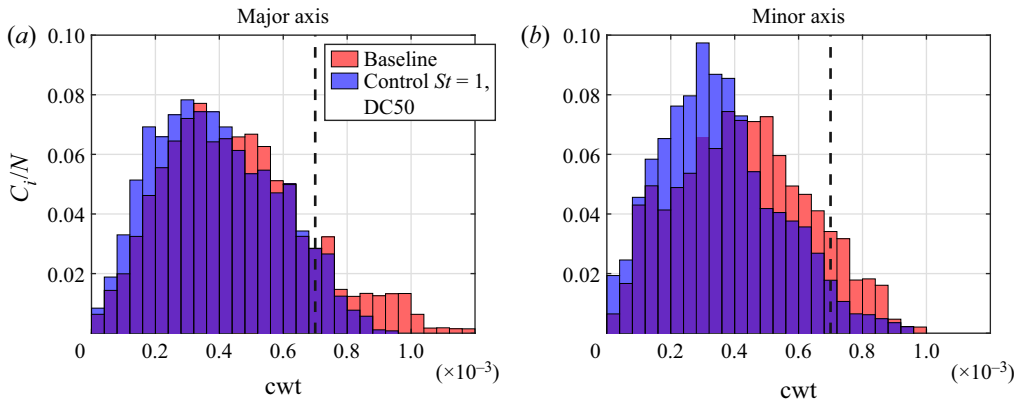
964 A11-28

Figure 20. Histograms depicting probability of occurrence of time-frequency localized events between $0.2 \leq St \leq 0.4$ at various scalogram magnitudes on (*a*) the major axis plane and (*b*) the minor axis plane. The dashed black line represents the threshold of the scalogram magnitude chosen to quantify a significant event.

probability of occurrence of time-frequency localized events between $0.2 \leq St \leq 0.4$ in the above-discussed scalograms. The dashed black line depicts a representative threshold chosen to indicate the presence of a highly energetic acoustic event. A threshold of 7×10^{-4} is used to identify significant acoustic events, which is near the upper limit of the contour levels shown in figure 19. Levels above this threshold are saturated red spots in figure 19, depicting localised high-intensity events. Therefore, bins to the right of the dashed line can be considered to be of interest, due to its impact on far-field OASPL. Comparing the baseline and the controlled jets on the two planes, the probability of occurrence of extreme acoustic events has been reduced through control. A reduction of about 78 % is seen on the major axis plane while a 51 % reduction is seen on the minor axis plane. The steep roll off of probability at high scalogram magnitudes in the controlled case shows that strong events leading to production of sound waves at energy-containing frequencies are reduced.

Thus, the control succeeds in creating a flow response conducive for noise mitigation by (*a*) reducing energy within the supersonic regime of peak radiating frequencies and redistributing it into an energy band at the forcing frequency, (*b*) exciting higher azimuthal modes and smaller spatial scales, and (*c*) reducing extreme intermittent events within the jet responsible for bursts of acoustic energy.

7. Effect on mean flow and turbulent statistics

For practical aspects related to scalability (Brown 2008) and sound modelling studies (Rosa 2018; Prasad & Gaitonde 2022), it is important to understand the effect of control on the mean flow features and the near-field flow statistics of the jet. Figure 21 shows the streamwise velocity comparison between the baseline and controlled ($St = 1$, DC50) case on the major axis (figure 21*a*) and minor axis (figure 21*b*) planes. A few key differences are discernible between the two cases. The core length in the controlled case is slightly longer. There are also differences in the shear layer thickness close to the nozzle exit and the rate of spreading of the shear layer. These differences in the mean flow properties including centreline velocity, half-widths and shear layer thickness between the controlled and baseline cases are quantitatively presented in figures 22, 23 and 24, respectively.
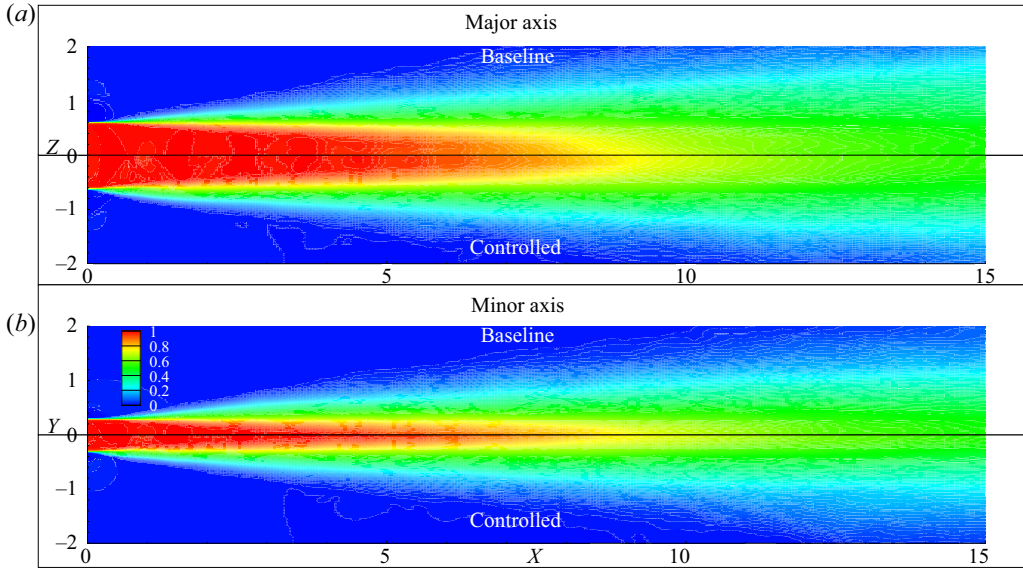
964 A11-29

Figure 21. Streamwise velocity contour comparison between baseline and controlled jet on (*a*) the major and (*b*) the minor axis planes.
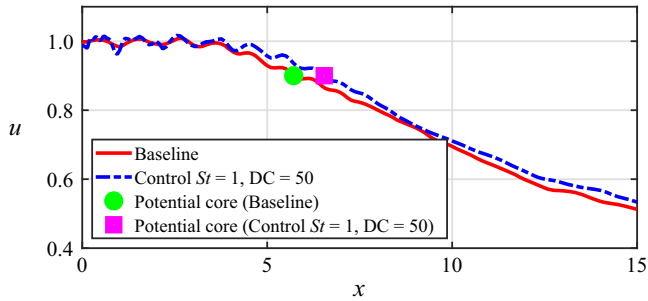

Figure 22. Centreline velocity comparison between the baseline and controlled jets. Potential core length in each case is marked as indicated.
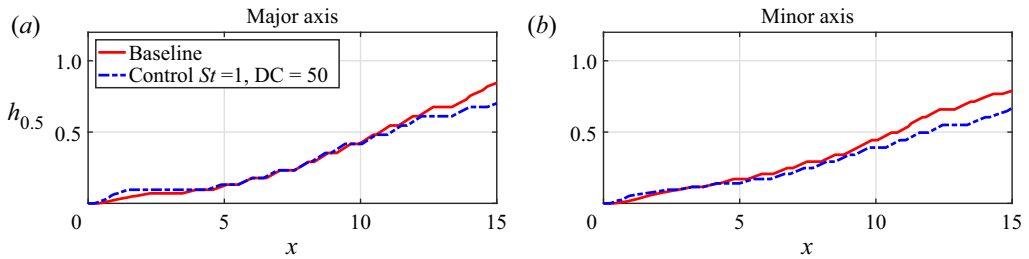

Figure 23. Half-width comparison between the baseline and controlled cases on (*a*) the major axis and (*b*) the minor axis.
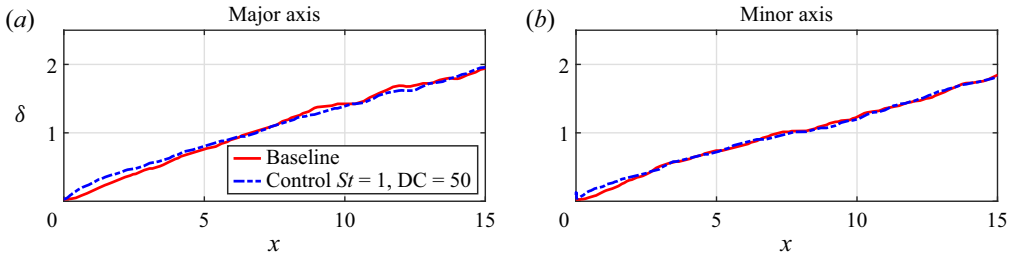
Figure 24. Shear layer thickness comparison between the baseline and controlled cases on (*a*) the major axis and (*b*) the minor axis.

Potential core length is calculated using the definition provided by Georgiadis & Papamoschou ([2003](#)) as, 'distance from jet exit to the axial station where the centreline velocity is 90 % of the primary nozzle exit velocity'. The estimate for the baseline jet is also verified using an analytical formulation provided for axisymmetric compressible jets by Witze ([1974](#)). Although the nozzle in this case is not axisymmetric, the mean flow exhibits largely axisymmetric features within about eight equivalent diameters downstream of the nozzle exit. The formulation is

$$\frac{x}{D_j} = \frac{0.70}{2\kappa\,(\rho_\infty/\rho_j)^{0.5}}, \quad \kappa = 0.063(M_j^2 - 1)^{-0.15}. \tag{7.1}$$

Replacing D_j with D_{eq}, using $M_j = 1.5$ and $\rho_j = \rho_\infty$ (perfectly expanded jet), the core collapse location is $x = 5.74$. This analytic value is very close to the numerical prediction, $x = 5.71$. The centreline velocity shows only minor variations between the two cases compared, as seen in figure 22. This includes slightly higher velocity oscillations near nozzle exit regions and a marginally lower centreline velocity decay, indicative of a slower rate of core collapse. The core collapse location estimate using the aforementioned definition for the controlled case is $x = 6.54$. Comparing the core collapse locations, the controlled jet core is longer by about $x \sim 0.8$ than the baseline jet, consistent with its lower centreline velocity decay rate and observations from the contours in figure 21.

The half-width ($h_{0.5}$) at a given streamwise location is defined as the corresponding transverse coordinate on the principal planes at which the mean streamwise velocity attains 50 % of its value at the jet centreline. Half-width plots on the major axis plane (figure 23*a*) and on the minor axis plane (figure 23*b*) reveal that the spreading rate of both jets are nearly the same from jet exit to about $x \sim 5$. A deviation from this trend for $x \geq 5$ is seen on the minor axis plane, where the baseline jet spreads at a relatively faster rate than the controlled jet. This deviation is also observed on the major axis plane further downstream for $x \geq 10$. The observation is consistent with the relatively longer potential core in the controlled jet, and also matches those of Huet *et al.* ([2009](#)), where lower centreline velocity decay rates were reported with pulsed micro-jet actuation in circular jets.

Figure 24(*a*,*b*) compares shear layer thickness (δ) development between the baseline and controlled jets on the major and minor axis planes, respectively. Shear layer thickness is defined as the (transverse coordinate) extent bounding streamwise velocity between 10 % and 90 % of the centreline velocity. On both the planes, excitation of coherent vortical features near the nozzle exit (see e.g. figure 13) results in a slightly thicker shear layer in the controlled jet for $x \leq 3$. Downstream of this location, both jets display nearly identical shear layer thicknesses.

The mean flow also provides an estimate of thrust impact associated with the control. While the 20 % duty cycle cases did not show any significant thrust variations from the baseline case, the thrust was reduced by approximately 0.93 % in the 50 % duty cycle cases. This change in thrust is comparable to that seen in fluid injector based control of circular jets by Prasad & Morris (2021), and control using micro vortex generators reported by Liu *et al.* (2022).

The phase-averaged and acoustically filtered variables analysed in the previous sections are inherently dominated by large-scale structures that have a direct impact on the acoustic radiation pattern. We now report turbulent kinetic energy (TKE) analysis to quantify the effects of control on plume turbulence, by encompassing all relevant fluctuation scales. It also has the potential to aid future efforts (that may involve other control concepts) in understanding the effects of manipulating near-field turbulence for achieving a desired change in far-field acoustics. This is accomplished by performing a budget of the TKE transport equation (7.2):

$$
\bar{\rho}\frac{Dk}{Dt} = \bar{\rho}C + \bar{\rho}P + \bar{\rho}\Pi - \bar{\rho}\epsilon + \bar{\rho}M + \bar{\rho}D,
$$

$$
\text{where}
$$

$$
k = \frac{\widetilde{u_i'' u_i''}}{2} : \text{TKE},
$$

$$
\bar{\rho}C = -\frac{\partial \bar{\rho}\widetilde{u_j}k}{\partial x_j} : \text{Mean flow convection},
$$

$$
\bar{\rho}P = -\overline{\rho u_i'' u_j''}\frac{\partial \widetilde{u_i}}{\partial x_j} : \text{TKE production},
$$

$$
\bar{\rho}\Pi = \overline{p'\frac{\partial u_i''}{\partial x_i}} : \text{TKE redistribution},
$$

$$
\bar{\rho}M = -\overline{\rho' u_i''}\left(\frac{\partial \bar{p}}{\partial x_i} - \frac{\partial \overline{\sigma_{ik}}}{\partial x_k}\right) : \text{Mass flux contribution},
$$

$$
\bar{\rho}\epsilon = \overline{\sigma_{ik}'\frac{\partial u_i''}{\partial x_k}} : \text{TKE dissipation},
$$

$$
\bar{\rho}D = -\frac{\partial}{\partial x_k}\left(\frac{\overline{\bar{\rho}u_i'' u_i'' u_k''}}{2} + \overline{p' u_k''}\delta_{ik} - \overline{\sigma_{ik}' u_i''}\right) : \text{TKE transport and diffusion}.
$$

(7.2)

In the above equation quantities with a bar ($\bar{q}$) represent Reynolds-averaged terms and quantities with a tilde ($\tilde{q}$) represent Favre-averaged terms. Fluctuations of quantities are represented as $q' = q - \bar{q}$ and $q'' = q - \tilde{q}$. The viscous stress tensor (σ_{ij}) is defined as $\sigma_{ij} = 2\mu(S_{ij} - S_{kk}\delta_{ij}/3)$, where $S_{ij} = \frac{1}{2}(\partial u_i/\partial x_j + \partial u_j/\partial x_i)$ is the strain rate tensor. Convergence of statistics is ensured by evaluating these using data segments of various temporal durations.

Streamwise variation of the dominant terms in the TKE equation along the nozzle lip line are shown in figure 25. The plots show comparison of quantities between the baseline jet (red solid line) and jet with control (blue dash-dot line) on the major axis (left column) and minor axis planes (right column). In the controlled jet, the azimuthal arrangement of actuators (see figure 1) is such that the principal planes bisect at least one actuator.
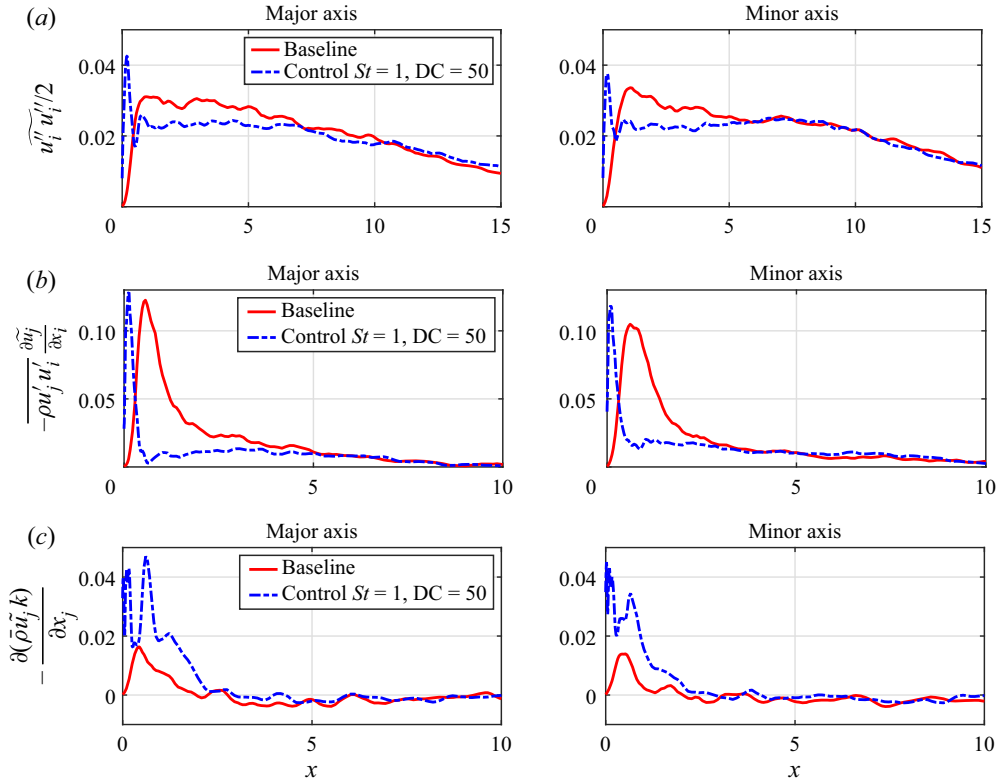
Figure 25. Streamwise variation at the nozzle lip line of (*a*) TKE, (*b*) TKE production and (*c*) TKE convection, in the baseline and controlled jets. The left and right columns correspond to results obtained on the major and minor axis planes, respectively.

Thus, the inner lip line of the nozzle is chosen to highlight the direct impact of actuation on turbulent statistics. Only those terms that showed significant differences between the baseline and controlled jets are included in these results.

Figure 25(*a*) shows the lip-line variation of TKE. The TKE of the baseline jet is relatively small but finite within the nozzle due to the imposed coloured pressure perturbations. Outside the nozzle, shear layer instabilities amplify and convect downstream, intensifying mixing and breakdown, leading to a rapid increase in TKE. As the shear layer spreads, TKE levels equilibrate and remain relatively constant until the core collapse location. Downstream of the core collapse, TKE levels display a quasi-linear decay. These results are similar to those observed by Bhide & Abdallah (2022) in the study of TKE budgets for perfectly expanded rectangular jets and Huet *et al.* (2009) in the study of micro-jet based control of circular jets. The effect of actuators in the controlled jet leads to a sharp concentration of TKE in the vicinity of the nozzle exit as a direct consequence of actuation. However, TKE levels rapidly decay to values lower than the baseline jet until the core collapses (which is slightly downstream of the baseline jet). Downstream of the potential core, both jets have a similar distribution of TKE, indicating that the influence of actuation on turbulent features are primarily limited to the spreading shear layer within the extent of the potential core. The above trends are similar on both principal planes, indicating that the actuation redistributes TKE into a very small region near to the nozzle exit. A similar observation was made by Prasad & Morris (2020) when

964 A11-33

studying fluid-inserts based control of circular jets. The aforementioned reduction in TKE levels for the controlled case can be understood as a consequence of two main mechanisms: TKE production and TKE convection.

The TKE production term is compared for the two jets in figure 25(*b*). For each plane considered, the term containing the planar spanwise gradient is the dominant production term (Lakshmi Narasimha Prasad *et al.* 2022*a,b*). This results from the large gradients across the shear layer, and strong correlation between streamwise and spanwise velocity fluctuations. Thus, we plot $-\overline{\rho u_j'' w''}(\partial \widetilde{u}_j / \partial z)$ on the major axis plane, and $-\overline{\rho u_j'' v''}(\partial \widetilde{u}_j / \partial y)$ on the minor axis plane. As expected, TKE production is largest near the nozzle exit regions, where the shear layer contains enhanced gradients and strong velocity fluctuations due to the amplification of shear layer instabilities. As the shear layer spreads and gradients decrease, the production term attenuates, eventually becoming negligible, preceding core collapse. The spike in TKE production in the controlled jet near the nozzle exit rapidly reduces to magnitudes below that in the baseline case. Although the spanwise gradient across the shear layer dominates the production term, the mean gradient levels were observed to reach comparable magnitudes within about $x \sim 2$ from the nozzle exit for both jets. Thus, the primary cause for attenuated TKE production levels is the reduced correlation between fluctuations in the streamwise and in-plane velocity components on the principal planes (i.e. reduction in Reynolds's stress).

Figure 25(*c*) shows the redistribution of TKE via convection. Convection peaks near regions of TKE production, from where the TKE is redistributed by either convection or diffusion. Turbulent kinetic energy convection follows the trends in TKE production. However, in the controlled jet, TKE convection levels are much higher than the baseline jet over the streamwise extent of the potential core. The lower production and higher convection results in reduced TKE levels in the controlled jet. Thus, the control technique has a significant impact on reducing turbulent fluctuation amplitudes in the region harbouring noise sources.

This study has thus identified key dynamics in the hydrodynamic and acoustic near fields of rectangular jets induced by LAFPA-based actuators, and the resulting impact on far-field noise mitigation. The insights from the parameter combinations tested can be leveraged to explore more optimal forcing and feedback-based control strategies in the future. Furthermore, these efforts can also benefit from linear perturbation theory tools, which can refine forcing signals, guided by sensitivities of the basic state.

8. Conclusion

This study addresses the relatively less explored problem of active noise control in non-axisymmetric jets, utilizing a high-fidelity computational approach. We utilize a LAFPA-based active control for a Mach 1.5 perfectly expanded jet, exiting a 2 : 1 AR rectangular nozzle. Based on prior experimental insights, the effects of control on noise mitigation and associated shear layer dynamics are studied for three frequencies ($St =$ 0.3, 1.0 and $St =$ 2.0) and two duty cycles (20 % and 50 %).

Forcing the jet at $St = 0.3$ leads to a global response at the column mode, and exacerbates the downstream super-directive radiation, resulting in significant increases in far-field noise levels up to 5 dB at peak radiating angles. The signature of $St = 1.0$ forcing manifests as a downstream propagating acoustic stream, resulting from periodic vortex intrusions into the potential core. In addition, an actuation signature appears as sideline radiation. The $St = 2.0$ forcing creates three distinct acoustic streams. This includes a downstream propagating stream resulting from supersonic convection of vortical waves in

the shear layer, a sideline stream directly emitted from the actuator and an interference stream of the above two.

The higher frequencies are effective in reducing far-field noise along the downstream direction. In all cases, actuator tones are prevalent along the sideline direction. Although the baseline jet has a mostly axisymmetric far-field acoustic signature, noise mitigation achieved by the actuators are asymmetric. Higher levels of noise mitigation are observed on the major axis plane, which also exhibits lower levels of actuator tones relative to the minor axis plane.

Among the tested frequencies, $St = 1$ is the most effective in noise mitigation, with a peak noise reduction of about 1.0 and 1.5 dB for DC = 20 % and DC = 50 %, respectively. Overall, $St = 1$, DC = 50 % has better insulation of the far field from actuator tones. Spectral comparison indicates that noise mitigation results from reduced energy levels at around $St \sim 0.3$, which corresponds to the jet column mode frequency, and around $St \sim 0.6$.

A detailed near-field analysis of $St = 1$, DC = 50 % is performed to understand causal mechanisms resulting in sound mitigation. The response of this shear layer to actuation highlights the formation of lambda vortices when the actuator is off, and a roller vortex when the actuator is on. Differential convection speeds lead to vortex interactions, where the head region of the hair pin vortex is pinched off and merges with the roller vortex. Eventually, a staggered array of azimuthally connected lambda vortices appear, energizing streamwise vortical elements in the turbulent plume, effectively reducing the noise generation mechanisms. Such a favourable outcome is not observed at the other frequencies tested. Column mode resonance at $St = 0.3$ forcing leads to the formation of large coherent structures at the scale of the plume, and associated super-directive noise radiation. The $St = 2$ forcing fails to elicit a coherent response in the shear layer, and has minimal impact in generating streamwise vorticity.

Effectiveness of $St = 1$, DC = 50 % control in reducing peak noise levels is explained through three key mechanisms. First, it reduces the energy within the supersonic regime of peak radiating frequencies and redistributes into an energy band at the forcing frequency. This is evident in the wavenumber–frequency spectra of the acoustic response of the jet. Second, higher azimuthal modes are excited at frequencies at which far-field noise reduction was observed. This is established using an azimuthal mode evaluation of the leading two spectral proper orthogonal modes extracted at the column mode of the jet. Redistribution of energy from the axisymmetric ϕ mode 0 to helical ϕ modes 1 and 2 causes the wave packet to reduce its radiative efficiency. Third, localized events within the plume responsible for bursts of acoustic radiation are reduced significantly in the controlled jet, as quantified using a time-frequency analysis.

Effects of actuation on the mean flow characteristics are minimal, which includes a slightly slower rate of velocity decay and, hence, a marginally longer potential core. Spreading rates post core collapse are also lower in the controlled jet. A budget analysis of TKE at the nozzle lip line reveals an upstream shift of regions with peak TKE, when imposing control. Production significantly reduces and convection increases, resulting in lower levels of TKE within the shear layer. This indicates significant impact of control on the region harbouring noise sources, leading to redistribution and attenuation of turbulent fluctuations.

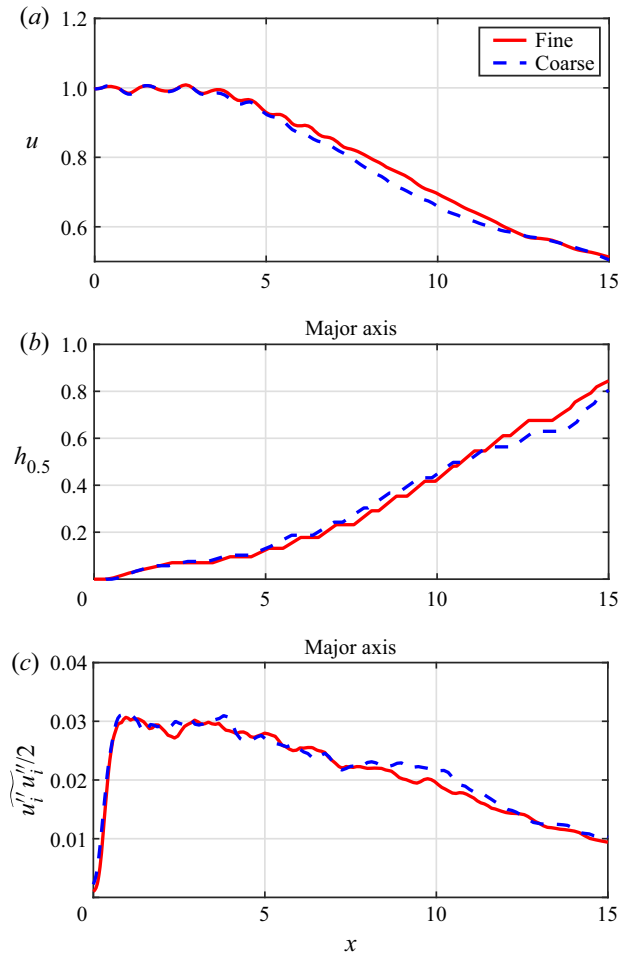**Declaration of interests.** The authors report no conflict of interest.

Figure 26. (*a*) Jet centreline velocity comparison, (*b*) half-width comparison on the major axis plane and (*c*) lip line TKE comparison on the major axis plane, between coarse and fine grids.

Author ORCIDs.

 Anirudh Lakshmi Narasimha Prasad https://orcid.org/0000-0001-7802-2208.

Appendix. Grid independence study

As mentioned in § 2, a grid convergence study is performed by comparing mean flow properties and flow statistics from simulations on a coarse and fine mesh. The approximate node count in the coarser grid is about 40.60×10^6 while that of the finer grid is about 47.53×10^6. The chosen grid spacing for the finer mesh is informed by previous simulations at similar Reynolds numbers, involving compressible jets exiting circular nozzles (Unnikrishnan & Gaitonde 2016), rectangular nozzles (Chakrabarti *et al.* 2021) and diamond nozzles (Lakshmi Narasimha Prasad *et al.* 2022*a*). The coarse mesh is around 10 % coarser in the streamwise direction, and around 20 % coarser along each of the transverse directions.

Figure 26(*a*) shows the centreline velocity comparison for the baseline jet simulated on the two grids. A close agreement is observed, with minor variations beyond the core

964 A11-36

collapse location. Figure 26(*b*) plots the half-width comparison on the major axis plane. The spreading rates of the two jets are essentially identical within the region of interest. Slight deviations are seen towards the end of the domain due to aggressive stretching of the coarser grid. Similar trends are seen on the minor axis plane as well, but are not included here for brevity.

Figure 26(*c*) shows the second-order statistical comparison of the jets on the two grids. The quantity chosen for comparison is the TKE at the jet lip line on the major axis plane. Large magnitudes of TKE closer to the nozzle exit and the quasi-linear decay in TKE magnitudes in the streamwise direction are captured on both grids accurately. These results are again consistent on both the principal planes of the nozzle.

REFERENCES

ADLER, M.C., GONZALEZ, D.R., STACK, C.M. & GAITONDE, D.V. 2018 Synthetic generation of equilibrium boundary layer turbulence from modeled statistics. *Comput. Fluids* **165**, 127–143.

ALVI, F.S., LOU, H., SHIH, C. & KUMAR, R. 2008 Experimental study of physical mechanisms in the control of supersonic impinging jets using microjets. *J. Fluid Mech.* **613**, 55–83.

ARNDT, R.E.A., LONG, D.F. & GLAUSER, M.N. 1997 The proper orthogonal decomposition of pressure fluctuations surrounding a turbulent jet. *J. Fluid Mech.* **340**, 1–33.

BHIDE, K. & ABDALLAH, S. 2022 Anisotropic turbulent kinetic energy budgets in compressible rectangular jets. *Aerospace* **9** (9), 484.

BLAZEK, J. 2001 *Boundary Conditions. Computational Fluid Dynamics: Principles and Applications*, 1st edn, p. 270. Elsevier Science.

BOGEY, C. & BAILLY, C. 2010 Influence of nozzle-exit boundary-layer conditions on the flow and acoustic fields of initially laminar jets. *J. Fluid Mech.* **663**, 507–538.

BRÈS, G.A., JORDAN, P., JAUNET, V., LE RALLIC, M., CAVALIERI, A.V.G., TOWNE, A., LELE, S.K., COLONIUS, T. & SCHMIDT, O.T. 2018 Importance of the nozzle-exit boundary-layer state in subsonic turbulent jets. *J. Fluid Mech.* **851**, 83–124.

BRIDGES, J. 2012 Acoustic measurements of rectangular nozzles with bevel. In *18th AIAA/CEAS Aeroacoustics Conference (33rd AIAA Aeroacoustics Conference)*, p. 2252. American Institute of Aeronautics and Astronautics.

BROWN, C. 2008 Scalability of the localized arc filament plasma actuators. In *14th AIAA/CEAS Aeroacoustics Conference (29th AIAA Aeroacoustics Conference)*, p. 3043. American Institute of Aeronautics and Astronautics.

CAVALIERI, A.V.G., JORDAN, P., COLONIUS, T. & GERVAIS, Y. 2012 Axisymmetric superdirectivity in subsonic jets. *J. Fluid Mech.* **704**, 388–420.

CAVALIERI, A.V.G., JORDAN, P. & LESSHAFFT, L. 2019 Wave-packet models for jet dynamics and sound radiation. *Appl. Mech. Rev.* **71** (2), 020802.

CHAKRABARTI, S., GAITONDE, D.V. & UNNIKRISHNAN, S. 2021 Representing rectangular jet dynamics through azimuthal fourier modes. *Phys. Rev. Fluids* **6** (7), 074605.

CHEN, N. & YU, H. 2014 Mechanism of axis switching in low aspect-ratio rectangular jets. *Comput. Maths Applics.* **67** (2), 437–444.

CODERONI, M., LYRINTZIS, A.S. & BLAISDELL, G.A. 2019 Large-eddy simulations analysis of supersonic heated jets with fluid injection for noise reduction. *AIAA J.* **57** (8), 3442–3455.

COLONIUS, T. & FREUND, J. 2002 Pod analysis of sound generation by a turbulent jet. In *40th AIAA Aerospace Sciences Meeting and Exhibit*, p. 72. American Institute of Aeronautics and Astronautics.

CRAWLEY, M. & SAMIMY, M. 2014 Decomposition of the near-field pressure in an excited subsonic jet. In *20th AIAA/CEAS Aeroacoustics Conference*, p. 2342. American Institute of Aeronautics and Astronautics.

CROW, S.C.J. & CHAMPAGNE, F.H. 1971 Orderly structure in jet turbulence. *J. Fluid Mech.* **48** (3), 547–591.

DOAK, P.E. 1989 Momentum potential theory of energy flux carried by momentum fluctuations. *J. Sound Vib.* **131** (1), 67–90.

DURCH, J.S., JOELLENBECK, L.M. & HUMES, L.E. 2006 *Noise and Military Service: Implications for Hearing Loss and Tinnitus*. National Academies.

GAITONDE, D.V. 2012 Analysis of the near field in a plasma-actuator-controlled supersonic jet. *J. Propul. Power* **28** (2), 281–292.

GAITONDE, D.V. & SAMIMY, M. 2010 Effect of plasma-based azimuthal mode excitation on supersonic jet flow. In *5th Flow Control Conference*, p. 4416. American Institute of Aeronautics and Astronautics.

GAITONDE, D.V. & SAMIMY, M. 2011 Coherent structures in plasma-actuator controlled supersonic jets: axisymmetric and mixed azimuthal modes. *Phys. Fluids* **23** (9), 095104.

GARMANN, D.J. 2013 Characterization of the vortex formation and evolution about a revolving wing using high-fidelity simulation. PhD thesis, University of Cincinnati.

GEORGIADIS, N. & PAPAMOSCHOU, D. 2003 Computational investigations of high-speed dual stream jets. In *9th AIAA/CEAS Aeroacoustics Conference and Exhibit*, p. 3311. American Institute of Aeronautics and Astronautics.

GHASSEMI ISFAHANI, A., WEBB, N.J. & SAMIMY, M. 2022 Effects of active control on flow and near-and far-field acoustics of twin rectangular supersonic jets. In *AIAA Scitech 2022 Forum*, p. 2401. American Institute of Aeronautics and Astronautics.

GOJON, R., GUTMARK, E.J. & MIHAESCU, M. 2019 Antisymmetric oscillation modes in rectangular screeching jets. *AIAA J.* **57** (8), 3422–3441.

GONZÁLEZ, D.R., GAITONDE, D.V. & LEWIS, M.J. 2015 Large-eddy simulations of plasma-based asymmetric control of supersonic round jets. *Intl J. Comput. Fluid Dyn.* **29** (3–5), 240–256.

GRINSTEIN, F.F. 1995 Self-induced vortex ring dynamics in subsonic rectangular jets. *Phys. Fluids* **7** (10), 2519–2521.

GUTMARK, E.J. & GRINSTEIN, F.F. 1999 Flow control with noncircular jets. *Annu. Rev. Fluid Mech.* **31** (1), 239–272.

GUTMARK, E.J., SCHADOW, K.C. & BICKER, C.J. 1990 Near acoustic field and shock structure of rectangular supersonic jets. *AIAA J.* **28** (7), 1163–1170.

HEEB, N.S., MORA SANCHEZ, P., GUTMARK, E.J. & KAILASANATH, K. 2013 Investigation of the noise from a rectangular supersonic jet. In *19th AIAA/CEAS Aeroacoustics Conference*, p. 2239. American Institute of Aeronautics and Astronautics.

HELFER, T.M. 2011 Noise-induced hearing injuries, active component, US armed forces, 2007–2010. *MSMR* **18** (6), 7–10.

HUET, M., FAYARD, B., RAHIER, G. & VUILLOT, F. 2009 Numerical investigation of the micro-jets efficiency for jet noise reduction. In *15th AIAA/CEAS Aeroacoustics Conference (30th AIAA Aeroacoustics Conference)*, p. 3127. American Institute of Aeronautics and Astronautics.

ISFAHANI, A.G., WEBB, N.J. & SAMIMY, M. 2021 Coupling modes in supersonic twin rectangular jets. *AIAA Paper* 2021–1292.

KEARNEY-FISCHER, M., SINHA, A. & SAMIMY, M. 2013 Intermittent nature of subsonic jet noise. *AIAA J.* **51** (5), 1142–1155.

KIBENS, V. 1980 Interaction of jet flowfield instabilities with flow system resonances. In *6th Aeroacoustics Conference*, p. 963. American Institute of Aeronautics and Astronautics.

KINZIE, K.W. 1995 Aeroacoustic properties of moderate reynolds number elliptic and rectangular supersonic jets. PhD thesis, The Pennsylvania State University.

KOENIG, M., CAVALIERI, A.V.G., JORDAN, P., DELVILLE, J., GERVAIS, Y. & PAPAMOSCHOU, D. 2013 Farfield filtering and source imaging of subsonic jet noise. *J. Sound Vib.* **332** (18), 4067–4088.

LAKSHMI NARASIMHA PRASAD, A., SALEH, Y., SELLAPPAN, P., UNNIKRISHNAN, S. & ALVI, F.S. 2022*a* Effects of expansion ratio and nozzle asymmetry on flowfield of diamond jets. *AIAA J.* **60** (9), 5215–5231.

LAKSHMI NARASIMHA PRASAD, A., SALEH, Y., SELLAPPAN, P., UNNIKRISHNAN, S. & ALVI, F.S. 2022*b* Near-field and far-field effects of heating in an over-expanded Mach 2 diamond jet. In *AIAA Scitech 2022 Forum*, p. 1152. American Institute of Aeronautics and Astronautics.

LAKSHMI NARASIMHA PRASAD, A. & UNNIKRISHNAN, S. 2023 Effect of LAFPA based control on supersonic rectangular jets. In *AIAA Scitech 2023 Forum*, p. 1346. American Institute of Aeronautics and Astronautics.

LEAHY, R.P., GHASSEMI ISFAHANI, A., WEBB, N.J. & SAMIMY, M. 2022 The effects of active control on near-field pressure fluctuations in supersonic rectangular twin jets. In *28th AIAA/CEAS Aeroacoustics 2022 Conference*, p. 2968. American Institute of Aeronautics and Astronautics.

LILLY, J.M. & OLHEDE, S.C. 2009 Higher-order properties of analytic wavelets. *IEEE Trans. Signal Process.* **57** (1), 146–160.

LILLY, J.M. & OLHEDE, S.C. 2012 Generalized morse wavelets as a superfamily of analytic wavelets. *IEEE Trans. Signal Process.* **60** (11), 6036–6041.

LIU, J., KHINE, Y.Y., SALEEM, M., LOPEZ RODRIGUEZ, O. & GUTMARK, E.J. 2021 Supersonic jet noise reduction using micro vortex generators. In *AIAA Aviation 2021 Forum*, p. 2183. American Institute of Aeronautics and Astronautics.

LIU, J., KHINE, Y.Y., SALEEM, M., LOPEZ RODRIGUEZ, O. & GUTMARK, E.J. 2022 Effect of axial location of micro vortex generators on supersonic jet noise reduction. In *AIAA Scitech 2022 Forum*, p. 1791. American Institute of Aeronautics and Astronautics.

LIU, X-D., OSHER, S. & CHAN, T. 1994 Weighted essentially non-oscillatory schemes. *J. Comput. Phys.* **115** (1), 200–212.

MARTENS, S. 2002 Jet noise reduction technology development at GE aircraft engines. *ICAS Paper* 842.

MICHALKE, A. & FUCHS, H.V. 1975 On turbulence and noise of an axisymmetric shear flow. *J. Fluid Mech.* **70** (1), 179–205.

PETERSEN, R.A. & SAMET, M.M. 1988 On the preferred mode of jet instability. *J. Fluid Mech.* **194**, 153–173.

POINSOT, T.J. & LELE, S.K. 1992 Boundary conditions for direct simulations of compressible viscous flows. *J. Comput. Phys.* **101** (1), 104–129.

PRASAD, C. & GAITONDE, D.V. 2022 A time-domain linear method for jet noise prediction and control trend analysis. *Aerosp. Sci. Technol.* **121**, 107377.

PRASAD, C. & MORRIS, P.J. 2020 A study of noise reduction mechanisms of jets with fluid inserts. *J. Sound Vib.* **476**, 115331.

PRASAD, C. & MORRIS, P.J. 2021 Steady active control of noise radiation from highly heated supersonic jets. *J. Acoust. Soc. Am.* **149** (2), 1306–1317.

RODRIGUEZ, D., PRASAD, C. & GAITONDE, D. 2021 Near-field turbulent structures in supersonic rectangular jets using 3D parabolized stability equations. In *AIAA Aviation 2021 Forum*, p. 2276. American Institute of Aeronautics and Astronautics.

ROE, P.L. 1981 Approximate Riemann solvers, parameter vectors and difference schemes. *J. Comput. Phys.* **43**, 357–372.

ROSA, V. 2018 Rans-based prediction of noise from isothermal and hot subsonic jets. PhD thesis, University of Southampton.

SAMIMY, M., KIM, J.-H., KASTNER, J., ADAMOVICH, I. & UTKIN, Y. 2007*a* Active control of a Mach 0.9 jet for noise mitigation using plasma actuators. *AIAA J.* **45** (4), 890–901.

SAMIMY, M., KIM, J.-H., KASTNER, J., ADAMOVICH, I. & UTKIN, Y. 2007*b* Active control of high-speed and high-Reynolds-number jets using plasma actuators. *J. Fluid Mech.* **578**, 305–330.

SAMIMY, M., KIM, J.-H. & KEARNEY-FISCHER, M. 2009 Active control of noise in supersonic jets using plasma actuators. In *Turbo Expo: Power for Land, Sea, and Air*, vol. 48821, pp. 97–107. American Institute of Aeronautics and Astronautics.

SAMIMY, M., KIM, J-H., KEARNEY-FISCHER, M. & SINHA, A. 2010 Acoustic and flow fields of an excited high Reynolds number axisymmetric supersonic jet. *J. Fluid Mech.* **656**, 507–529.

SCHMIDT, O.T. & COLONIUS, T. 2020 Guide to spectral proper orthogonal decomposition. *AIAA J.* **58** (3), 1023–1033.

SEROR, C., SAGAUT, P., BAILLY, C. & JUVÉ, D. 2000 Sound generated by high speed rectangular jet using large eddy simulation. In *Office National D Etudes Et De Recherches Aerospatiales Onera-Publications-TP*. American Institute of Aeronautics and Astronautics.

SHIH, C., KROTHAPALLI, A. & GOGINENI, S. 1992 Experimental observations of instability modes in a rectangular jet. *AIAA J.* **30** (10), 2388–2394.

SHU, C.W. & OSHER, S. 1988 Efficient implementation of essentially non-oscillatory shock-capturing schemes. *J. Comput. Phys.* **77** (2), 439–471.

SINHA, A., RODRÍGUEZ, D., BRÈS, G.A. & COLONIUS, T. 2014 Wavepacket models for supersonic jet noise. *J. Fluid Mech.* **742**, 71–95.

SNYDER, R. 2007 Mixing control in supersonic rectangular jets using plasma actuators. PhD thesis, The Ohio State University.

SPETH, R.L. & GAITONDE, D.V. 2013 Parametric study of a Mach 1.3 cold jet excited by the flapping mode using plasma actuators. *Comput. Fluids* **84**, 16–34.

STEPHENS, D.G. & MAYES, W.H. 1979 Aircraft noise-induced building vibrations. In *Community noise*. ASTM International.

TAM, C.K.W. 2019 A phenomenological approach to jet noise: the two-source model. *Phil. Trans. R. Soc.* A **377** (2159), 20190078.

TAM, C.K.W. & BURTON, D.E. 1984*a* Sound generated by instability waves of supersonic flows. Part 1. Two-dimensional mixing layers. *J. Fluid Mech.* **138**, 249–271.

TAM, C.K.W. & BURTON, D.E. 1984*b* Sound generated by instability waves of supersonic flows. Part 2. Axisymmetric jets. *J. Fluid Mech.* **138**, 273–295.

TAM, C.K.W., GOLEBIOWSKI, M. & SEINER, J. 1996 On the two components of turbulent mixing noise from supersonic jets. In *Aeroacoustics conference*, p. 1716. American Institute of Aeronautics and Astronautics.

TAM, C.K.W. & MORRIS, P.J. 1980 The radiation of sound by the instability waves of a compressible plane turbulent shear layer. *J. Fluid Mech.* **98** (2), 349–381.

TAM, C.K.W., PASTOUCHENKO, N.N. & VISWANATHAN, K. 2005 Fine-scale turbulence noise from hot jets. *AIAA J.* **43** (8), 1675–1683.

TINNEY, C.E. & JORDAN, P. 2008 The near pressure field of co-axial subsonic jets. *J. Fluid Mech.* **611**, 175–204.

TOWNE, A., SCHMIDT, O.T. & COLONIUS, T. 2018 Spectral proper orthogonal decomposition and its relationship to dynamic mode decomposition and resolvent analysis. *J. Fluid Mech.* **847**, 821–867.

UNNIKRISHNAN, S., CAVALIERI, A.V.G. & GAITONDE, D.V. 2019 Acoustically informed statistics for wave-packet models. *AIAA J.* **57** (6), 2421–2434.

UNNIKRISHNAN, S. & GAITONDE, D.V. 2016 Acoustic, hydrodynamic and thermal modes in a supersonic cold jet. *J. Fluid Mech.* **800**, 387–432.

VALENTICH, G., UPADHYAY, P. & KUMAR, R. 2016 Mixing characteristics of a moderate aspect ratio screeching supersonic rectangular jet. *Exp. Fluids* **57** (5), 1–14.

VELTIN, J. & MCLAUGHLIN, D. 2009 Flow field and acoustic measurements of rectangular supersonic jets. In *47th AIAA Aerospace Sciences Meeting including The New Horizons Forum and Aerospace Exposition*, p. 19. American Institute of Aeronautics and Astronautics.

VISWANATH, K., JOHNSON, R.F., CORRIGAN, A.T., KAILASANATH, K., MORA SANCHEZ, P., BAIER, F. & GUTMARK, E.J. 2016 Noise characteristics of a rectangular vs circular nozzle for ideally expanded jet flow. In *54th AIAA Aerospace Sciences Meeting*, p. 1638. American Institute of Aeronautics and Astronautics.

WELCH, P. 1967 The use of fast fourier transform for the estimation of power spectra: a method based on time averaging over short, modified periodograms. *IEEE Trans. Audio Electroacoust.* **15** (2), 70–73.

WIEGAND, C. 2018 F-35 air vehicle technology overview. In *2018 Aviation Technology, Integration, and Operations Conference*, p. 3368. American Institute of Aeronautics and Astronautics.

WITZE, P.O. 1974 Centerline velocity decay of compressible free jets. *AIAA J.* **12** (4), 417–418.

YONG, J.S.-E. & WANG, D.-Y. 2015 Impact of noise on hearing in the military. *Mil. Med. Res.* **2** (1), 1–6.

ZAMAN, K.B.M.Q. 1996 Axis switching and spreading of an asymmetric jet: the role of coherent structure dynamics. *J. Fluid Mech.* **316**, 1–27.